

A characteristic scale for cold gas

Michael McCourt,¹† S. Peng Oh,¹ Ryan O’Leary² and Ann-Marie Madigan^{2,3}

¹Department of Physics, University of California, Santa Barbara, Santa Barbara, CA 93106, USA

²JILA, University of Colorado, Boulder, CO 80309, USA

³Department of Astrophysical and Planetary Sciences, University of Colorado, Boulder, CO 80309, USA

Accepted 2017 October 12. Received 2017 October 12; in original form 2016 October 7

ABSTRACT

We find that clouds of optically thin, pressure-confined gas are prone to fragmentation as they cool below $\sim 10^6$ K. This fragmentation follows the lengthscale $\sim c_s t_{\text{cool}}$, ultimately reaching very small scales (~ 0.1 pc/ n), as they reach the temperature $\sim 10^4$ K at which hydrogen recombines. While this lengthscale depends on the ambient pressure confining the clouds, we find that the column density through an individual fragment $N_{\text{cloudlet}} \sim 10^{17} \text{ cm}^{-2}$ is essentially independent of environment; this column density represents a characteristic scale for atomic gas at 10^4 K. We therefore suggest that ‘clouds’ of cold, atomic gas may, in fact, have the structure of a mist or a fog, composed of tiny fragments dispersed throughout the ambient medium. We show that this scale emerges in hydrodynamic simulations, and that the corresponding increase in the surface area may imply rapid entrainment of cold gas. We also apply it to a number of observational puzzles, including the large covering fraction of diffuse gas in galaxy haloes, the broad-line widths seen in quasar and AGN spectra and the entrainment of cold gas in galactic winds. While our simulations make a number of assumptions and thus have associated uncertainties, we show that this characteristic scale is consistent with a number of observations, across a wide range of astrophysical environments. We discuss future steps for testing, improving and extending our model.

Key words: MHD – plasmas – ISM: clouds – Galaxy: centre – Galaxy: halo.

1 INTRODUCTION

One of the unique features of astrophysical plasmas relative to terrestrial fluids is the presence of *multiphase gas*, which spans a wide range of density and temperature. Whereas local density fluctuations of $\lesssim 1$ per cent might be typical for the air in our atmosphere, cooling in astrophysics can lead to gas spanning orders of magnitude in density. Multiphase gas occurs everywhere from cosmological scales such as the circumgalactic medium (CGM) permeating galaxy haloes on ~ 100 kpc scales, to comparatively tiny scales such as the interstellar medium in galaxy discs on ~ 10 pc scales, and all the way down to compact objects such as the broad-absorption line regions around accreting massive black holes on scales of $\sim (0.01 - 0.1)$ pc. The dynamics of multiphase gas thus enters into the evolution of a wide range of cosmic structures and its formation and evolution are important topics of study.

This paper focuses on optically thin multiphase gas, especially in the temperature range between 10^4 and 10^6 K, where radiation by atomic lines can rapidly cool the gas. We focus our attention on long-lived clouds, which are confined by external pressure or by magnetic fields. We do not consider transient, unconfined clouds

(such as fluctuations due to supersonic turbulence), or self-gravitating gas (e.g., in the intergalactic medium or in giant molecular clouds and star-forming regions). Though our assumptions may sound restrictive, we find such conditions are frequently met. We discuss several applications of our results in Sections 3 and 4.

When modelling the cold component of multiphase gas, it is often assumed that the cold gas is composed of monolithic, contiguous ‘clouds’. This assumption is not always motivated, however, and it may lead to a number of the persistent inconsistencies related to the cold gas in galaxies. In particular:

(i) Absorption- and emission-line studies of the CGM on large scales in galaxy haloes often find a relatively small amount of cold gas, with a high density and therefore small total volume, yet also with a very high covering fraction (e.g. Hennawi et al. 2015; see Section 3.1 for more references). In other words, a tiny total amount of cold gas somehow manages to span the entire galaxy; it is difficult to understand how so little gas can be present everywhere. (Even this small volume of cold gas is however far larger than predicted in most cosmological simulations, however.)

(ii) Strongly supersonic turbulence is sometimes needed to explain the broad-line widths seen in cold gas (see Section 3.2 for references and examples). But such motions are difficult to understand theoretically because supersonic turbulence should shock, rapidly either dissipating the motions or heating the gas above line-emitting

*E-mail: mkmccjr@gmail.com (MM); peng@physics.ucsb.edu (SPO)

†Hubble Fellow.

temperatures. Outside of dense star-forming regions, with rapid cooling and continual stirring, strongly suprathermal line widths are hard to explain.

(iii) Galactic winds often contain entrained cold gas moving at high velocity. This is not a priori expected, however, because the time-scale for a wind to destroy cold gas via shear instabilities is typically much shorter than the time-scale to accelerate the cold gas via drag forces. Though observations of such comoving multiphase gas are quite common, they remain unexplained (this is the ‘*entrainment in trouble*’ problem; Zhang et al. 2017).

(iv) High-resolution observations of atomic clouds in our own galaxy halo, such as high-velocity clouds (HVCs), indicate that the clouds are made up of many small fragments or filaments with scales less than 0.1 pc (and possibly much smaller). At least in regions which are not self-gravitating, no explanation for this small lengthscale currently exists.

(v) The broad-line region (BLR) and broad-absorption line (BAL) region around quasars exhibit elements of *all* of the above problems. These regions are made of gas in close proximity (~ 0.01 – 0.1 pc) to the quasar: this gas orbits with relativistic velocities ($\gtrsim 0.1c$) and experiences an intense field of ionizing radiation. Even under such extreme conditions, some fraction of the gas remains cold and neutral, creating the low-energy atomic lines for which these regions are named. Several lines of evidence suggest that these lines come from a large number of dense, small cloudlets with a tiny overall volume-filling fraction (see Section 3.3 for references and details). To our knowledge, no theoretical explanation currently exists for this tiny size, or for the enormous number of cloudlets required to match the measured line profiles.

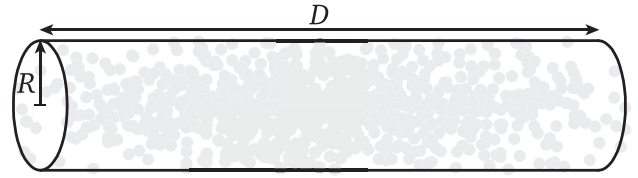
We discuss each of these problems in more detail in Section 3, where we suggest that all of them stem at least in part from an assumption that cold gas comes in the form of monolithic, contiguous clouds.

In this paper, we show that gas clouds larger than a characteristic scale $\ell_{\text{cloudlet}} \sim c_s t_{\text{cool}} \sim (0.1 \text{ pc})/n$ are prone to fragmentation, where c_s is the sound speed for cold gas, t_{cool} is the cooling time and n is its volume density in cm^{-3} (see Section 2 for details). For large clouds with an initial size $R_0 \gg \ell_{\text{cloudlet}}$, this fragmentation is so rapid that we refer to it as *shattering*.

In all of the examples mentioned above – CGM, HVCs, BALs, and galactic winds – we find that the scale ℓ_{cloudlet} is orders of magnitudes smaller than the size of the system. Hence, we propose that ‘clouds’ of cold gas in these systems should be modelled in a manner analogous to meteorological *clouds*: they are composed of tiny droplets (or ‘cloudlets’) of dense gas distributed sparsely throughout space, with a low overall volume-filling fraction. Physically, dividing gas into many tiny cloudlets decouples its area-covering fraction from the volume-filling fraction (or total mass) of the gas: the ratio of the area-covering fraction f_A to the volume-filling fraction f_V becomes:¹

$$\frac{f_A}{f_V} \sim \frac{D}{\ell_{\text{cloudlet}}}$$

where ℓ_{cloudlet} is the size of an individual cloudlet and D is the size of the system of cloudlets (we sketch this geometry in Fig. 1). We



$$\begin{aligned} M_H/m_H &= N_H R^2 = N_{\text{clumps}} n_H \ell^3 \\ f_V &= n_{\text{clump}} \ell^3 = N_H / (n_H D) \\ f_A &= (D/\ell) f_V \end{aligned}$$

$M_H \equiv$ cold mass	$m_H \equiv$ proton mass
$N_H \equiv$ cold column density	$n_H \equiv$ cold volume density
$R \equiv$ beam size	$D \equiv$ system size
$\ell \equiv$ cloudlet size	$n_{\text{clump}} \equiv$ cloudlet density
$f_V \equiv$ volume filling fraction	$f_A \equiv$ area covering fraction

Figure 1. Sketch of a line of sight through a galaxy with virial radius D and a pixel size R . Shows the relations among observable quantities.

show in Section 3 that this ratio D/ℓ_{cloudlet} may be very large in astrophysical systems.

This paper is organized as follows. In Section 2, we discuss the physics of shattering and our interpretation of the scale ℓ_{cloudlet} . We also show simulations demonstrating how this scale emerges in numerical simulations. In Section 3, we discuss some observational evidence for shattering: we show how a large area-to-volume ratio $f_A/f_V \gg 1$ is precisely what quasar-absorption studies of the CGM in galaxy haloes imply (Section 3.1). We also find evidence for shattering in the broad, turbulent line-widths sometimes found in the interstellar and circumgalactic media (Section 3.2), as well as in the broad-line regions around quasars, some aspects of which seem to imply very small clouds (Section 3.3), and in high-resolution observations of HVCs and other Milky Way clouds (Section 3.4). We also suggest that a large ratio $f_A/f_V \gg 1$ may explain the observed entrainment of cold gas in galaxy winds (Section 3.5). We summarize our model in Section 4 and discuss more speculative applications, such as the rapid evolution of the escape fraction during the epoch of reionization and the observation that the Milky Way has an $\sim 10 \times$ lower CGM mass than other comparable galaxies (Section 4.2). We discuss our assumptions and theoretical uncertainties in this section (Section 4.1), as well as directions for further work (Section 4.2).

2 THE PHYSICS OF SHATTERING

In this section, we discuss physical reasons why we might expect cold gas in astrophysics to sometimes come in the form of tiny cloudlets dispersed throughout a much larger volume. We begin with a qualitative discussion in Section 2.1 and then demonstrate shattering using preliminary numerical simulations in Section 2.2. While we note that our numerical results are somewhat uncertain, we compare our results with a range of observations in Section 3 and with recent laboratory experiments in Section 4.

¹ We define the area-covering fraction f_A somewhat crudely as the mean number of cloudlets intercepted along a line of sight through the multiphase gas. Thus, f_A can be >1 , and often $f_A \gg 1$. This is related to, but not identical to, observable quantities such as the statistics of sightlines covered as a function of column density.

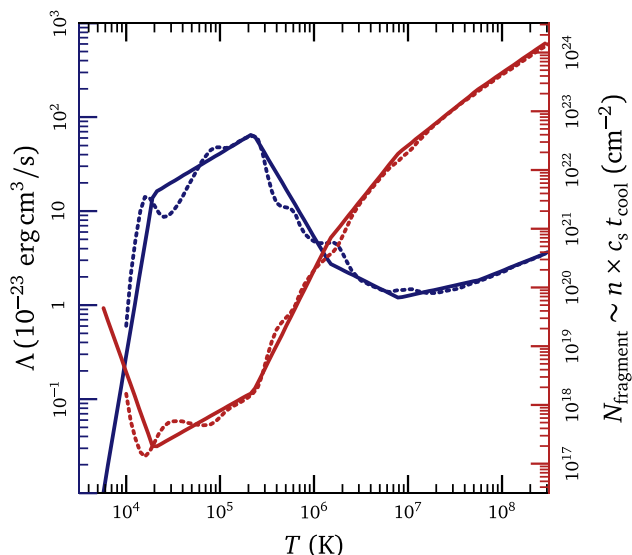


Figure 2. (blue): Cooling curve for collisionally ionized, solar-metallicity gas. The dotted curve shows the calculation from Sutherland & Dopita (1993), and the solid curve shows a simplified piecewise power-law fit used in our simulations (Section 2.2). Gas below $\sim 10^6$ K cools rapidly down to $\sim 10^4$ K. Such rapid cooling fragments the gas, implying a small fragment size, measured here by the column density through an individual fragment, $N_{\text{cloudlet}} \sim n \times c_s t_{\text{cool}}$, shown in the red curve (see equation 1 in Section 2.1). As before, the dotted line is calculated from Sutherland & Dopita (1993) and the solid line is calculated from the simplified piecewise power-law fit used in our simulations.

2.1 Intuitive discussion

The processes creating cold gas likely vary with application: the cool CGM in galaxy haloes, for example, may have an entirely different physical origin than the atomic gas in the broad-line regions around a quasar. We expect our results apply to the dynamics of cold gas in general, regardless of its exact (and often unknown) origin. For concreteness, however, in this section we imagine gas cooling out of a hot, ambient medium, as might be produced by thermal instability (e.g. Field 1965). We focus on the final non-linear outcome of thermal instability, which is not directly predicted from the linear analysis in Field’s classic work. Our results are complementary to Meerson (1989)’s non-linear extension to Field (1965)’s work, but as we discuss below, we focus on much longer wavelength modes, which we show to have qualitatively different behaviour. Fig. 2 shows the cooling curve (blue) for collisionally ionized,² solar-metallicity gas computed by Sutherland & Dopita (1993). When gas cools below $\sim 10^6$ K, line emission can rapidly cool the gas down to $\sim 10^4$ K. Such rapid cooling between 10^6 and 10^4 K naturally suggests a two-phase medium, consisting of a hot phase with $T \gtrsim 10^6$ K alongside a cold phase with $T \lesssim 10^4$ K. This is especially true if some heating process is present to offset the (slow) cooling in the hot phase and maintain it indefinitely.

Fig. 3 illustrates some gas cooling out of a hot, pressure-supported background. If the cooling perturbation has an initial size $R_0 \gg c_s t_{\text{cool}}$, where c_s is the sound speed (at which pressure forces are communicated throughout the cloud), and t_{cool} is the cooling time (the time-scale for the cloud to radiate away its energy), then the

perturbation cannot contract as quickly as it loses its pressure support. It is commonly assumed (e.g. Field 1965; Burkert & Lin 2000) that such perturbations cool *isochorically*, i.e. at constant density, with little change to the size or shape of the cloud. The cloud is then severely out of pressure balance, but contracts only on longer time-scales, reaching pressure equilibrium after the (far longer) sound-crossing time. We sketch this process in the top path of Fig. 3. However, such a configuration is vastly out of force balance and is therefore extremely unstable. The stable state is for cooling gas to reach $\sim 10^4$ K, and to be in (at least approximate) pressure balance with its surroundings; we emphasize that for initially large clouds, the isochoric route represents an extremely slow path to equilibrium.

The fastest route to equilibrium is for the gas to split into smaller pieces, each of which contracts more rapidly.³ If the gas breaks into many separate pieces, each with a scale $\sim c_s t_{\text{cool}}$, such pieces are small enough to cool isobarically, essentially never leaving pressure balance with their surroundings. These fragments contract as they radiate away their energy, but since they are out of sonic contact with one another, each piece cools independently and they pull away from each other as they contract. The result is something analogous to a mist or a fog, in which dense, small cloudlets are spread throughout the volume and a hot, interstitial medium permeates the space between the cloudlets. We sketch this process in the bottom path of Fig. 3: here, the cloud reaches equilibrium after only a cooling time, *far* faster than implied by the isochoric route discussed above.

For gas above 10^4 K, we note that the lengthscale $c_s t_{\text{cool}}$ plummets $\sim T^3$ as the gas cools (see the red curve in Fig. 2). Each of the fragments in the bottom picture of Fig. 3 may therefore fragment again to yet smaller scales, and again, repeatedly, until the gas reaches the stable temperature near 10^4 K. This splitting therefore pushes to smaller scales as the gas cools, eventually reaching the scale where $c_s t_{\text{cool}}$ is minimized. Putting in a characteristic density, we find:

$$\ell_{\text{cloudlet}} \sim \min(c_s t_{\text{cool}}) \sim (0.1 \text{ pc}) \left(\frac{n}{\text{cm}^{-3}} \right)^{-1}, \quad (1)$$

where we have used the Sutherland & Dopita (1993) cooling curve, as shown in Fig. 2. Since the cloudlet scale $\ell_{\text{cloudlet}} \propto 1/n$, the column density through an individual cloudlet

$$N_{\text{cloudlet}} = n \ell_{\text{cloudlet}} \sim 10^{17} \text{ cm}^{-2} \quad (2)$$

is essentially independent of the surrounding environment; we will apply this useful result later in Section 3. We note that this discussion is very similar to that in Voit & Donahue (1990), who arrive at an identical minimum column density N_{cloudlet} .

While we evaluate equation 1 at the temperature where $c_s t_{\text{cool}}$ is minimized, we note that one or more secondary processes may also influence the cloudlet size (such as shock-heating; see Fig. A3 in Appendix A). Despite a factor of $\lesssim 10$ uncertainty in the shattering scale for cold gas, it is orders of magnitude smaller than the typical sizes for systems of cold gas, and below the scales usually probed in simulations or in observations. This is all that is needed for our basic conclusions.

³ Though we have not specified the dynamics leading to this splitting, it would ultimately stem from compression by the ambient hot medium. We expect the unbalanced pressure serves as a source of free energy to drive fluid motions or instabilities on a wide range of scales, even if the detailed processes are not yet identified.

² We discuss the possible impact of photoionization in Section 4.1.

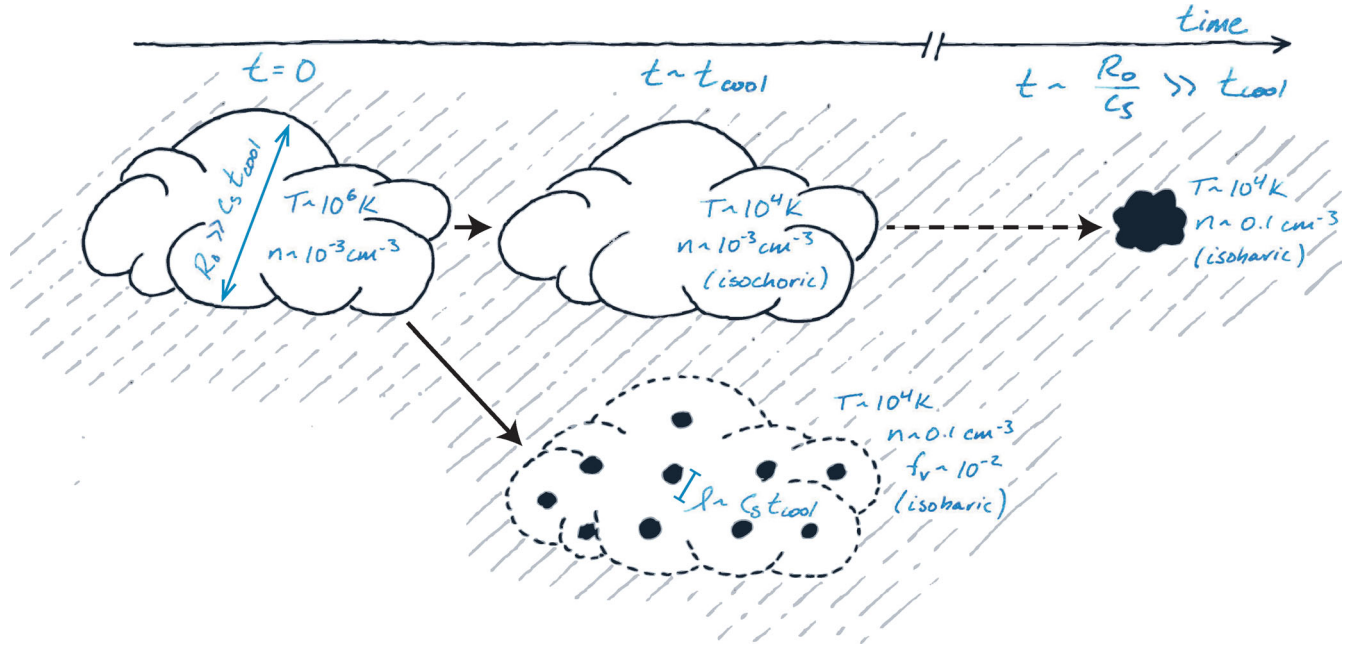


Figure 3. The fastest path to equilibrium is to shatter. We imagine a cooling perturbation with an initial size $R_0 \gg c_s t_{\text{cool}}$ embedded within an ambient medium, represented by grey hatching. (*top route*): It is commonly assumed (e.g. Field 1965; Burkert & Lin 2000) that such a perturbation will cool isochorically, reaching 10^4 K after one cooling time, with little change in the cloud size or density. The resulting cloud is severely underpressured and out of equilibrium; it contracts on the (much larger) sound-crossing time-scale, only afterwards reaching pressure equilibrium. (*bottom route*): A much more direct path to pressure equilibrium is for the cloud to fragment into smaller pieces, each with a scale $\sim c_s t_{\text{cool}}$; such fragments can cool isobarically, never leaving equilibrium. (Not shown.) As these fragments cool, the lengthscale $c_s t_{\text{cool}}$ shrinks; when this happens, the clumps fragment to yet smaller scales, never deviating dramatically from pressure equilibrium.

The fragmentation we discuss here is closely analogous to the Jeans instability, which describes the collapse of pressure-supported gas due to self-gravity (Jeans 1901; Low & Lynden-Bell 1976). In this case, clouds smaller than a characteristic lengthscale:

$$\lambda_J \sim c_s t_{\text{dyn}} \sim \frac{c_s}{\sqrt{G\rho}}$$

can communicate pressure forces on a time-scale faster than the free-fall time; such clouds therefore establish hydrostatic equilibrium, in which forces due to pressure balance those due to gravity. Small clouds resist collapse in this way, instead undergoing stable oscillations about an equilibrium configuration. Clouds larger than this scale cannot communicate pressure forces rapidly enough to establish hydrostatic equilibrium, however; with no way to balance gravity, large clouds are therefore susceptible to collapse. Since regions separated by distances $\gtrsim \lambda_J$ are out of causal contact as they collapse, each contracts independently, fragmenting the cloud into distinct chunks of mass $M_J \sim \rho \lambda_J^3$. The ‘shattering’ process we sketch in Fig. 3 is similar to the Jeans instability, with contraction driven by cooling and external pressure, rather than self-gravity; the fragmentation driven by these two processes is otherwise substantially identical.

This analogy with the Jeans instability extends further: in isothermal gas, relevant for dense star-forming regions, the Jeans mass $M_J \sim \rho \lambda_J^3 \propto \rho^{-1/2}$ decreases as the gas contracts to higher density. Gas therefore continually fragments to smaller scales as it collapses. The final core size is determined by the scale at which the gas becomes optically thick, such that its contraction is no longer isothermal; above this density, the Jeans mass increases with density and the gas becomes stable to further fragmentation. Physically, this transition represents the smallest possible scale for $\lambda_J(\rho, T[\rho])$,

and results in core masses $\sim M_J^{(\text{min})} \ll 1 M_\odot$, rather than the initial value $\sim M_J^{(\text{init})} (1 \text{ cm}^{-3}, 100 \text{ K}) \sim 10^5 M_\odot$ characteristic of the ISM. The fragmentation cascade we describe in this paper is qualitatively similar to Jeans’ fragmentation; in our picture, pressure-confined gas follows the scale $c_s t_{\text{cool}}(T) \sim T^3$ as it decreases along the cooling curve, ultimately reaching a stable, minimum scale near 10^4 K. We therefore expect the relevant scale for cold gas is the *minimum* value of $c_s t_{\text{cool}}$, not simply its initial value.

This point highlights an essential difference between our scenario and the theories presented by Burkert & Lin (2000) and by Hennebelle & P  rault (1999), who also identify a scale $\sim c_s t_{\text{cool}}$ in multiphase gas. These theories are conceptually somewhat different, however, and focus on the early development of thermal instability producing the cold gas. These theories therefore evaluate $c_s t_{\text{cool}}$ in the hot medium, *before* the gas cools, and assume that large perturbations cool isochorically, before being compressed monolithically by their surroundings, such that $l_{\text{cold}} \sim (c_s t_{\text{cool}})^{(\text{hot})} \times \delta^{-1/3}$, where $\delta \equiv \rho_{\text{cool}}/\rho_{\text{hot}}$ is the volume contraction ratio. We instead suggest that cooling drives continued fragmentation, and therefore that $c_s t_{\text{cool}}$ should be evaluated in the cold phase, near the temperature where this scale is minimized. By analogy with Jeans’ instability, if the gas cools down to $\sim 10^4$ K, we expect it will fragment to this minimum scale. Thus, the scale ℓ_{cloudlet} can be significantly smaller than the scales identified by Burkert & Lin (2000) and Hennebelle & P  rault (1999). In the following section, we show how this small physical lengthscale appears in high-resolution numerical simulations with rapid cooling. We furthermore show that the scale ℓ_{cloudlet} does not depend on the initial temperature of the cooling gas; this is consistent with the repeated fragmentation discussed above, but not with the scales predicted by Burkert & Lin (2000) and by Hennebelle & P  rault (1999).

2.2 Simulation results

We numerically study multiphase gas via simulating thermal instability, which exponentially amplifies small temperature fluctuations and thus *produces* multiphase gas and ‘cloud-crushing’, which studies the interaction between hot and cold gas phases and therefore probes the detailed evolution of multiphase gas after it forms.⁴

We note that cloud crushing and the dynamics of multiphase gas are thorny problems to study numerically, and that we have not controlled for several numeric errors which may be present in our simulations (see Appendix B and Section 4.1 for a discussion). Our simulations presented here are only meant to be suggestive, and must be followed with a more detailed study.

2.2.1 Thermal instability and forming multiphase gas

Fig. 4 shows a perturbation cooling out of a hot medium, analogous to the scenario sketched in Fig. 3. The top panel shows our initial condition. White shows an ambient, $\sim 10^7$ K background, and grey fluff shows an isobaric perturbation at $\sim 10^6$ K, which will cool down to $\sim 10^4$ K.⁵ These are 2D hydro simulations evolved using the second-order, Godunov-type code *Athena* (Gardiner & Stone 2008; Stone et al. 2008). We use the Sutherland & Dopita (1993) cooling curve, implemented via the Townsend (2009) algorithm, and we run the simulations long enough for the $\sim 10^6$ K gas to cool, but not long enough for the $\sim 10^7$ K gas to cool appreciably. With this choice of parameters, we have a well-defined hot phase which remains hot, and we avoid any need for ‘feedback’ heating to stave off a cooling catastrophe. We detail our computational set-up in Appendix A.

When we make the domain size large compared to $c_s t_{\text{cool}}$, as shown in the second panel of Fig. 4, the perturbation shatters into tiny fragments. Here, the simulation domain is full of tiny dots of cold gas. In order to emphasize this point, the red squares mark apparently diffuse regions of the domain. Zooming in on these regions, shown in the insets, reveals that they are full of cloudlets with a low-volume filling fraction and a tiny characteristic size which is unresolved in this simulation. If these cloudlets eventually disperse (e.g., due to turbulence), the result would be qualitatively very similar to the ‘fog’ of cloudlets discussed in the previous section.

When we make the domain size much smaller, comparable to the expected cloudlet size $\ell_{\text{cloudlet}} \sim c_s t_{\text{cool}}$, as shown in the bottom panel, we see no such fragmentation. In this case, the entire perturbation contracts as one coherent piece, and the gas assembles into a single, monolithic cold mass. The simulations in Fig. 4 therefore suggest that cold gas *forms* as a collection of distributed small chunks, each with a characteristic scale $\sim c_s t_{\text{cool}}$: perturbations much larger than this lengthscale shatter into smaller pieces, while perturbations smaller than this typical lengthscale maintain their integrity and

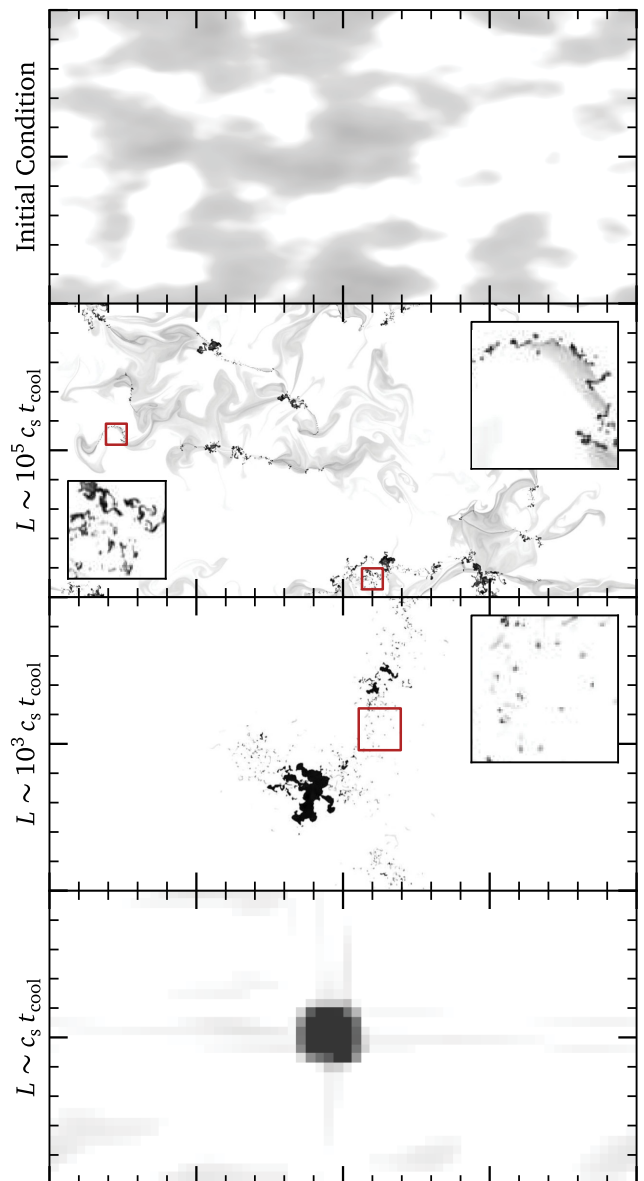


Figure 4. Cold clouds likely form small in the first place. These simulations show an initial perturbation (top panel) cooling down to 10^4 K. When the domain size is large ($\sim \text{kpc}$; second panel), the perturbation shatters into tiny fragments with a characteristic scale $c_s t_{\text{cool}}$, as discussed in Section 2.1. When the domain size is small, of order $\sim c_s t_{\text{cool}}$ (bottom panel), we see no such fragmentation. Instead, the cloud assembles into a monolithic blob. As argued in the text, these simulations suggest that $c_s t_{\text{cool}}$ is a characteristic lengthscale for cold gas: perturbations much larger than this scale fragment into much smaller pieces, while perturbations smaller than this lengthscale evolve coherently as effectively single objects. The third panel shows an intermediate case in which the cloud shatters and then re-forms as the cloudlets coagulate. This result may be unrealistic, however; we discuss it further in Section 2.2.1.

behave as single objects as they cool (see also the discussion of Fig. 5).

We show an intermediate case in the third panel of Fig. 4. Here, the perturbation initially cools and shatters into tiny fragments (some of which are shown in the inset). But mixing between the hot and cold phases cools the interstitial hot gas, lowering its pressure and driving the cloudlets together. In this simulation, the cold cloudlets will all eventually collect into a single blob. We note that this behaviour

⁴ Deeply nested AMR simulations such as those used to study star formation and cosmological structure formation can cover a fantastic range of scales, $\gtrsim 10^6$. However, this technique does not lend itself to the fog-like distribution of cold gas discussed here, with rapidly moving cloudlets widely distributed throughout the domain.

⁵ We start with a large density perturbation so as to get a distinct cloud which will cool without needing thermal instability to grow it from small amplitude; the physics of thermal instability is application-dependent and can be sensitive to assumptions about, e.g., stratification and background heating (see e.g. Field, Goldsmith & Habing 1969 for a theory relevant to the interstellar medium, or McCourt et al. 2012 for a model relevant to halo gas in massive galaxies and galaxy clusters). While important, the question of where cold gas comes from is beyond the scope of this paper.

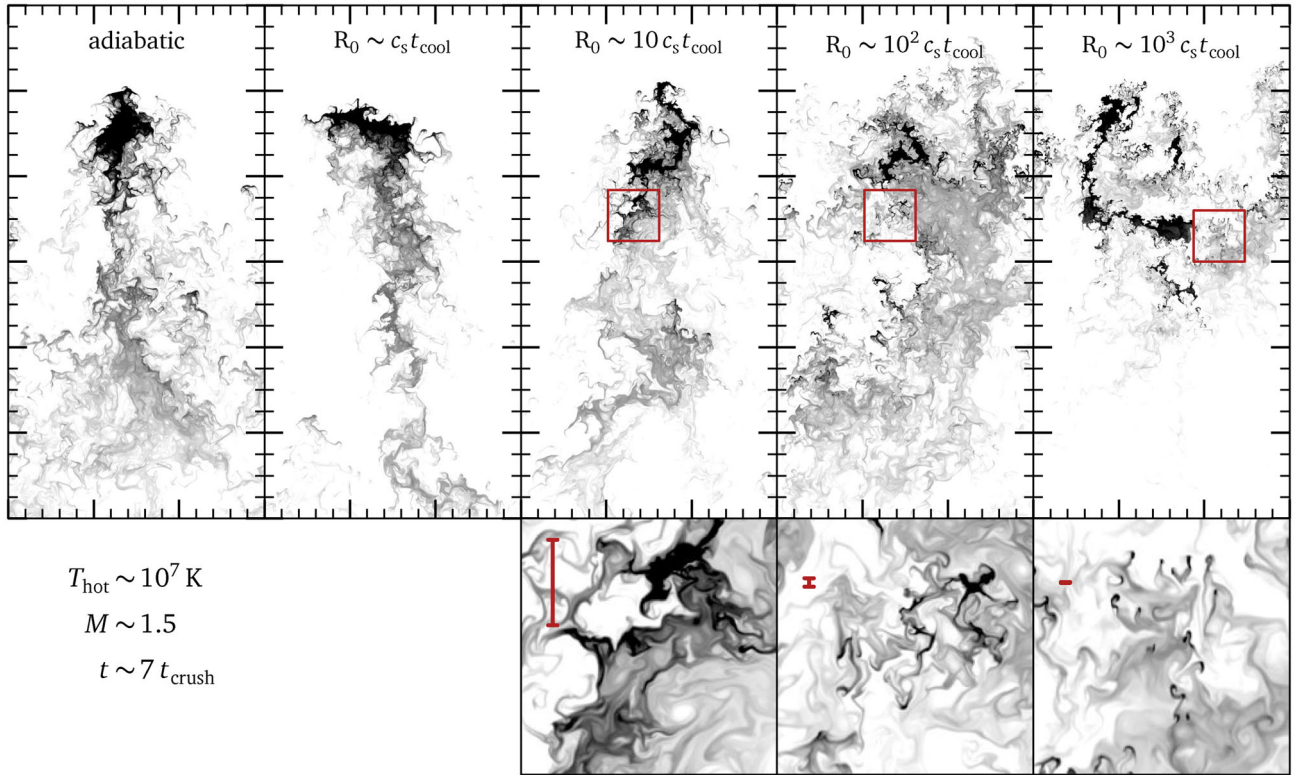


Figure 5. Clouds with initial sizes R_0 much greater than the characteristic size $c_s t_{\text{cool}}$ easily fragment into smaller pieces. Each panel shows a 2D hydrosimulation of an initially cold ($\sim 10^4$ K) cloud moving through an ambient medium at $\sim 10^7$ K. We resolve the initial cloud radius with 300 cells; see Fig. A1 for a resolution study. The initial size of the cloud decreases by a factor of 10 in each panel moving to the left. The rightmost panel shows a cloud with an initial size $10^3 \times c_s t_{\text{cool}}$; this would be a \lesssim kpc-sized cloud near the disc of the Milky Way, or out in the halo of a quasar host at redshift $z \sim 2$. The bottom panel, when shown, is a zoom-in of the red box in the top panel. Red error bars make the size $c_s t_{\text{cool}}$; when they are resolved by the simulation, the cloudlets roughly track this lengthscale. We detail the simulation set-up in Appendix A. These simulations are 2D and neglect both magnetic fields and viscosity; they cannot adequately model the disruption of the clouds. None the less, they do show that cooling breaks self-similarity in the cloud-crushing process and introduces a characteristic scale for the cold gas.

depends on mixing between the hot and cold phases, however, which is not resolved in this simulation. Moreover, this coagulation might easily be suppressed by turbulent motions, which are expected in a realistic astrophysical environment, but neglected in our simulations. Hence, we suspect this coagulation is an artefact of our simplified set-up; we defer a more detailed consideration of this intermediate case to a future study.

2.2.2 Cloud ‘crushing’ and evolution of multiphase gas

The simulations shown in Fig. 4 suggest that cold gas initially forms as small fragments within a much larger group, like the water droplets in a fog. Even if we somehow start with a large, monolithic cloud, however, such a cloud may *still* shatter into much smaller fragments. We show examples of this fragmentation in Fig. 5. In these 2D simulations, a sphere of dense gas at 10^4 K interacts transsonically with a hot, 10^7 K wind with a relative mach number of $v/c_s^{(\text{hot})} = 1.5$. (This set-up is roughly appropriate for our intended applications; we show in Appendix A that we obtain similar results for other choices of the parameters.) Running these simulations in 2D enables us to use resolutions of up to ~ 600 cells per cloud radius, significantly higher than the resolutions ~ 32 – 64 cells per cloud radius typical of state-of-the-art cloud-crushing simulations in 3D (e.g. Scannapieco & Brüggén 2015). We discuss in Appendix B why such high resolution is essential to study shattering. While the hydrodynamic instabilities which disrupt the cloud may behave

differently in 2D and 3D, we note that nothing about the shattering discussed in Section 2.1 seem fundamentally 3D. We therefore expect our results to be meaningful, despite being 2D. We will study shattering using 3D simulations in O’Leary et al. in preparation, and we compare our results with published 2D and 3D simulations in Appendix B. As before, we detail the rest of our computational set-up in Appendix A.

When the clouds in Fig. 5 interact with their surroundings, they disrupt due to a combination of cloud ‘crushing’ and shear instabilities (e.g. Klein, McKee & Colella 1994). However, in simulations with very high resolution and with strong cooling, we find that when the cloud disrupts, the cold material does not simply mix into the wind and disappear. Instead, at least in the set-up we tested, the cloud disrupts by fragmenting into tiny, dense, clumps. We will show these clumps follow the same characteristic scale ℓ_{cloudlet} discussed above.

The rightmost column in Fig. 5 shows a cloud with an initial size $\sim 10^3 c_s t_{\text{cool}}$; this would be an \sim kpc-sized cloud near the Milky Way disc, or out near the virial radius of a quasar host at redshift $z \sim 2$. We chose this scale because it is comparable to inferred sizes for large HVCs (Wakker & van Woerden 1997), or to the resolution limit in cosmological zoom-in simulations (e.g., Liang, Kravtsov & Agertz 2016; note that cosmological simulations have comparatively poor resolution in low-density halo gas). When this cloud disrupts, material strips off its surface and forms a turbulent wake behind the cloud. We find this wake is filled with little, unresolved

chunks of cold gas: as in Fig. 4, the inset zooms in on the region marked with the red square, showing that this apparently diffuse region is indeed filled with tiny dots of cold gas. For comparison, the red error bar in the inset shows the scale $c_s t_{\text{cool}}$, which is invisible at the scale of this figure.

Resolving the cloudlets in this simulation would be extremely expensive with our computational set-up; instead, we study the small-scale evolution by decreasing the initial cloud size. This reduces the dynamic range between the initial cloud and the final shattering fragments, making it easier to resolve the whole shattering process. Moving to the left, the second panel of Fig. 5 shows a simulation of a $10 \times$ smaller cloud. The shattering fragments are now marginally resolved (see the convergence study in Fig. A1), and the evolution is qualitatively very similar to that shown in the first panel. The cloudlets now appear to track the lengthscale $\sim c_s t_{\text{cool}}$ marked by the red error bar. The third panel shows a cloud smaller by yet another factor of 10. In this case, the evolution appears qualitatively different: here, the cloud does not shatter into tiny pieces. The cloud still fragments, however, and features in its wake seem to track the lengthscale $c_s t_{\text{cool}}$; we note that this interpretation is uncertain because there are only a small number of fragments and because this simulation may lack the dynamic range needed to capture the shattering discussed in Section 2.1.

Continuing to the left in Fig. 5, we show a cloud with an initial size $R_0 \lesssim c_s t_{\text{cool}}$, comparable to the expected size of the shattering fragments. Here, we see no fragmentation into smaller cloudlets. While the cloud disrupts due to shear instabilities, its wake does not contain dense knots of gas as seen in previous panels. The overall evolution is very similar to the adiabatic simulation shown in the final (leftmost) panel of Fig. 5. As in Fig. 4, this again suggests that the lengthscale $\sim c_s t_{\text{cool}}$ is a characteristic scale for cold gas in these simulations: clouds significantly larger than this scale fragment into much smaller pieces, while clouds comparable in size to this scale do not.

We note that the simulations shown in the leftmost panels of Fig. 5 are essentially identical to ‘cloud crushing’ simulations with weak or no cooling (e.g. Klein et al. 1994). Therefore, the cloud will eventually erode due to hydroinstabilities on a time-scale $\sim (\rho_{\text{cloud}}/\rho_{\text{wind}})^{1/2} \ell_{\text{cloudlet}}/v_{\text{wind}}$, which is extremely short due to the tiny size of the cloudlet. One might therefore conclude that shattering does little to influence the disruption of cold clouds: even if the cold gas passes through a phase consisting of tiny cloudlets, it will none the less rapidly mix into the ambient surroundings once these cloudlets disrupt. However, it is important to realize that the single-cloud simulation shown in the leftmost panel of Fig. 5 is not likely representative of a full system of cloudlets. In a full simulation of a large cloud, as shown in the rightmost panels of Fig. 5, the cloudlets rapidly become comoving with the ambient hot gas, and also shield one another from the full force of the background flow. These effects substantially reduce the velocity shear which shreds the isolated cloudlet in the leftmost panel of Fig. 5.

We illustrate this shielding in Fig. 6, which shows a simulation of a large number of cloudlets distributed with a volume-filling factor $f_v \sim 2 \times 10^{-2}$. Each (initially square) cloudlet is resolved by $(64)^2$ cells to ensure that they are not artificially stabilized by numerical viscosity and have sufficient resolution to disrupt. We report time in units of this single-cloud crushing time-scale. When we drive a wind into the upper edge of the domain, the cloudlets disrupt, but do not immediately mix into their surroundings. Instead, the dynamics of this population of cloudlets is more complex, and the cold gas ends up largely comoving with the hot phase (*bottom-right plot*). This likely results from both cloudlets shielding one another, and from

mixed material which re-cools in the cloudlet wakes, perhaps aided by streaming instabilities. We will delve into this process in more detail in future work. We note that, for cloudlets with a lengthscale $R_0 \sim c_s t_{\text{cool}}$, the ratio of the cooling time to the cloud-crushing time is:

$$\frac{t_{\text{cool}}}{t_{\text{crush}}} \sim \frac{v}{c_s}; \quad (3)$$

therefore, we might expect cloudlets to preferentially survive in subsonic regions of the flow. The lower-left plot in Fig. 6 indeed suggests that this is the case. The simulation in Fig. 6 is only meant to be suggestive, and we will perform a more detailed study in the future. In particular, it remains to be shown that this result holds in three dimensions.

We close this section by noting that Fig. A3 in the Appendix shows simulations similar to those in Fig. 5, but with a density ratio of 100 and a background temperature of 10^6 K. Though the cloud disruption proceeds differently in these simulations due to the different density ratio, the cloudlets ultimately fragment to a similar lengthscale. This independence of the initial temperature is consistent with the fragmentation cascade discussed in Voit & Donahue (1990) and in Section 2.1, but not with models based on linear theory such as those discussed in Field et al. (1969), Hennebelle & Péroul (1999) and Burkert & Lin (2000).

3 OBSERVATIONAL EVIDENCE FOR SHATTERING

In this section, we outline several applications of shattering to unexplained observations of cold gas. We discuss galaxy halo gas, ranging from the cold CGM probed by absorption studies of galaxies (Section 3.1), as well as HVCs and other resolved clouds in the Milky Way (Section 3.4), to the broad-line profiles seen in the circumgalactic and interstellar media (Section 3.2), to the atomic gas near quasars (Section 3.3), and to multiphase galactic winds, in which gas components with a wide range of densities and temperatures are frequently found to be comoving (Section 3.5).

3.1 Galaxy halo gas

The gas in the outskirts of galaxy haloes consists partly of cosmic gas which accretes from the intergalactic medium and shocks to the ($\gtrsim 10^6$ K in local $\sim L_*$ galaxies) virial temperature of the halo (Birnboim & Dekel 2003), and partly of gas recycled from the galaxy disc in a galactic ‘fountain’ (e.g. Shapiro & Field 1976; Oppenheimer et al. 2010). Both simulations and analytic arguments suggest this halo gas persists as a long-lived, virialized, approximately hydrostatic atmosphere in the haloes of galaxies more massive than $\sim 10^{12} M_\odot$ (e.g. White & Rees 1978; Birnboim & Dekel 2003; van de Voort et al. 2011; Fielding et al. 2017). This reservoir of gas in galaxy haloes seems to represent a significant fraction of the universe’s baryons (Maller & Bullock 2004; Stocke et al. 2013; Werk et al. 2014), and may supply the fuel necessary to explain continued star formation in galaxies (e.g. Bauermeister, Blitz & Ma 2010; Genzel et al. 2010).

Since the virialized, $\sim 10^6$ K component of halo gas is too faint to observe directly in emission,⁶ galaxy halo gas is instead studied in

⁶ Though this virialized CGM gas is invisible to current telescopes, there is little reason to doubt its existence: both analytic studies (e.g. White & Rees 1978; Birnboim & Dekel 2003; Maller & Bullock 2004) and cosmological simulations (e.g. van de Voort et al. 2011; Nelson et al. 2013; Fumagalli

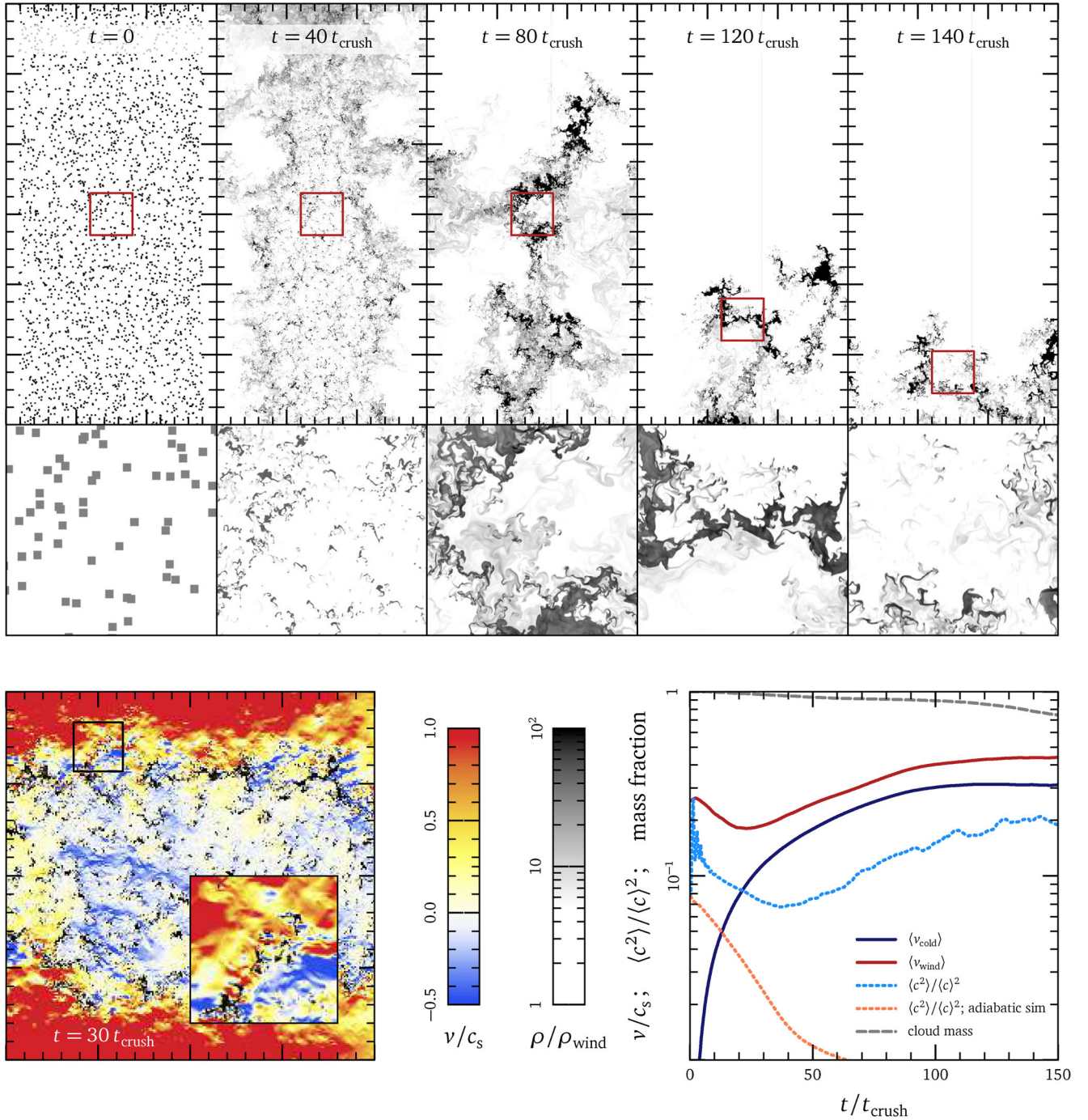


Figure 6. Entrainment of a system of cloudlets. (*top plot*): This figure shows a 2D simulation of a large number of cloudlets being hit with a wind coming from the top of the page. The simulation has an aspect ratio of 4:1; here we show the middle half. We resolve each (initially square) cloudlet with $(64)^2$ cells; this is sufficient for the cloudlets to disrupt due to cloud crushing or shear instabilities. While the cloudlets are disturbed by the incoming flow, and many partially disrupt, we find that the cold gas does not rapidly mix into the ambient hot wind. The cold gas moves around, coalesces and breaks apart again; however, the clumping factor remains relatively high, and the cold gas effectively entrains in the ambient wind. (*bottom right plot*): Quantitative evolution of the simulation. We demonstrate entrainment by showing the mean velocity of cloud (blue) and wind (red) gas. Note that the dynamics are not well-represented by an average velocity, however; see the colour plot on the left. We also show clumping factors for the above simulation (blue, dashed; note that the figure above shows only half of the simulation domain), and for an analogous simulation without cooling (orange, dashed) computed using passively advected scalars. Clumping factors become inaccurate metrics of cloud disruption once an appreciable fraction of cloud material leaves the domain (grey, dashed). (*bottom left plot*): Velocity distribution for wind gas, showing the central 1/4 of the domain. Red shows movement in the mean wind direction; blue shows a back-flow which develops within the bulk of the cloudlets. Most of the interstitial flow between cloudlets is sub-sonic. Cold gas may re-assemble due to streaming instabilities, which collect gas in converging flows in the wakes of dense knots. This figure is only meant to be suggestive; in particular, it remains to be shown that this entrainment works in 3D. We will investigate these dynamics further in a future study.

Table 1. Observations of atomic gas in the CGM. Though the CGM has no clear boundaries, in the interest of simplicity we attempt to show only bound gas in the outskirts of galaxy halos, at distances $\sim(0.5-1) r_{\text{vir}}$; we list more distant observations in the second group of rows and discuss closer-in observations with HVCs in Section 3.4. Most of these measurements come from photoionization modeling of absorption in sightlines to background quasars. In a few cases, further constraints come from fluorescent $\text{Ly}\alpha$ emission, from gravitationally lensed background quasars which probe structure in the plane of the sky, or from collisionally excited fine-structure lines; details are given in the notes below the table. The first group of columns shows properties closely related to observable quantities; this includes the mass and redshift of the galaxy, its virial radius, and the total column of neutral hydrogen (which sets the depth of absorption lines). The second group of columns shows properties derived from photoionization modeling; while there may be significant uncertainty in this modeling, in all cases the modeling indicates cold gas with a high density and tiny volume-filling fraction f_V . The final group of columns lists predictions based on the shattering described in this paper; overall, we find excellent agreement with the observations, both in terms of the high density and small scale for the gas, and in terms of the large number of clouds along the line of sight, needed to explain broad-line widths (see Section 3.2, below). The lone exception to this is Werk et al. (2014); the low high-column density N and low-volume density n they report yields entirely different results. The study by Werk et al. (2014) shows the only low-redshift observations we consider in this section, and are likely seeing a different phenomenon than the high- z observations; we discuss this in Section 4.

z	Observationally derived			Photoionization modeling				Shattering fragments		
	$M_{\text{halo}} (M_{\odot})$	$r_{\text{vir}} (\text{kpc})$	$N_{\text{HI}} (\text{cm}^{-2})$	$N_{\text{H}} (\text{cm}^{-2})$	$n_{\text{H}} (\text{cm}^{-3})$	f_V	$l_{\text{cold}} (\text{pc})$	$n_{\text{cold}} (\text{cm}^{-3})$	$\ell_{\text{cold}} (\text{pc})$	f_A
<i>Bound gas near the virial radius:</i>										
2.0 ^a	$10^{12.5}$	75	$10^{18.0}$	$10^{20.5}$	3	$10^{-3.5}$	34	1.1	$10^{-1.0}$	$10^{3.5}$
2.0 ^b	$10^{14.5}$	350	$10^{19.2}$	$10^{20.4}$	2	$10^{-4.0}$	41	24	$10^{-2.5}$	$10^{3.5}$
2.4 ^c	$10^{13.3}$	111	$10^{18.6}$	$10^{20.0}$	1.8	$10^{-4.0}$	18	10	$10^{-2.0}$	$10^{3.0}$
2.0 ^d	$10^{12.5}$	75	$10^{19.2}$	$10^{19.5}$	100	$10^{-6.0}$	0.2	1.1	$10^{-1.0}$	316.2
1.4 ^{e,†}			$10^{19.1}$	$10^{19.1}$	5	—	$\begin{cases} 0.5^{(\text{II})} \\ 135^{(\text{L})} \end{cases}$	—	—	125.9
0.8 ^{f,†}	(galaxy not detected)		—	$10^{17.8}$	0.1	—	2	—	—	6.3
3.5 ^{g,†}			$10^{16.0}$	$10^{17.8}$	0.2	—	$\begin{cases} 1.6^{(\text{II})} \\ 26^{(\text{L})} \end{cases}$	—	—	6.3
0.04 ^{h,§}	$10^{12.4}$	280	$10^{14.8}$	$10^{17.0}$	$10^{-3.5}$	$10^{-3.5}$	80	$10^{-2.5}$	23.7	1.0
<i>Low-pressure systems, likely out in the IGM:</i>										
2.4 ^{i,†}	$10^{11.5}$	28	$10^{16.4}$	$10^{19.0}$	$10^{-2.0}$	$10^{-2.0}$	324	(ambient		100.0
2.5 ^{j,†}	$10^{11.4}$	24	$10^{15.2}$	$10^{18.4}$	$10^{-2.5}$	$10^{-2.0}$	163	pressure		25.1
2.3 ^{k,†,‡}	—	—	—	—	$10^{-3.5}$	—	100	unknown)		—
<i>Low-redshift, qualitatively distinct from shattering:</i>										
0.2 ^l	$10^{12.0}$	183	$10^{16.5}$	10^{20}	$10^{-4.0}$	1.8	$\sim r_{\text{vir}}$	$10^{-2.5}$	31.0	~ 1

Notes. ^aLau et al. (2016) H I absorption (median values from sample)
^bHennawi et al. (2015) H I fluorescence + absorption
^cProchaska & Hennawi (2009) H I absorption, C II* & Si II* ('C' component)
^dLau et al. (2016) H I absorption, C II* (J1420+1603)
^eChurchill et al. (2003) H I absorption; gravitationally lensed quasar
^fRigby, Charlton & Churchill (2002) Fe II/Mg II, C IV/Mg II (systems 7, 13, & 18)
^gRauch et al. (1999) H I, O I/C II, Si II/Si IV; gravitationally lensed quasar
^hStocke et al. (2013) absorption (PKS 1302-102)
ⁱCrighton, Hennawi & Prochaska (2013) H I, C II, Si II, Mg II absorption
^jCrighton et al. (2015) absorption; multiple lines from Mg II – C IV
^kSchaye, Carswell & Kim (2007) absorption
^lWerk et al. (2014) COS halos

[†]Indicates an overall absorption system that resolves into individual components, each with approximately thermal line widths. In this case, the numbers N and n represent the thinnest resolved component, rather than the system as a whole. We see narrow lines only when the inferred number of clouds f_A along the line of sight (last column) is small.

[‡]By design, Schaye et al. (2007) report only conservative upper limits for the hydrogen column density. In this table, we quote only their conservative upper limit for l_{cold} .

[§]Stocke et al. (2013) show a wide range of different absorbing systems. Here, we show only PKS 1302-102; this is representative of absorbers close to the virial radius. Of absorbers in the range $(0.7-1.25) r_{\text{vir}}$, 13/14 show $10^{17} \text{ cm}^{-2} \lesssim N_{\text{H}} \lesssim 10^{18.5} \text{ cm}^{-2}$.

absorption along sightlines to more distant quasars. One particularly surprising development in this area has been the frequent finding

et al. 2014; Fielding et al. 2017) consistently predict its presence, and stacked observations have directly detected virialized gas in galaxies only slightly more massive than the Milky Way (Planck Collaboration XI 2013; Anderson, Churazov & Bregman 2015). Furthermore, circumstantial evidence from the confinement of gas clouds and stripping of satellite galaxies also points to a virialized CGM (e.g. Maller & Bullock 2004; Fang, Bullock & Boylan-Kolchin 2013; Stocke et al. 2013).

that the cool CGM in the outskirts of galaxy haloes comes in the form of dense ($\sim 1 \text{ cm}^{-3}$), small ($\sim 1-100 \text{ pc}$) clouds distributed throughout the halo. Though this cool CGM gas extends out to cosmological scales, as far out as the virial radius of the halo, it is comparable in density to the interstellar medium in the disc of the Milky Way galaxy! This unexpected result appears to be typical of the CGM, at least at the redshifts $z \gtrsim 2$ most accessible to quasar-absorption studies: Table 1 summarizes a number of such observations, all of which arrive at this basic conclusion. The first group of columns in Table 1 lists system properties closely related

to observable quantities: this includes the mass⁷ and redshift of the galaxy halo, along with the column density of neutral hydrogen.⁸ The second group of columns in Table 1 lists results derived from photoionization modelling, which yields the *total* hydrogen column density N_{H} , along with the volume density n_{H} , of the cold gas. The ratio of these densities $l_{\text{cold}} \equiv N_{\text{H}}/n_{\text{H}}$ provides an estimate of the total path length of cold gas along the line of sight. In all cases, this path length $l_{\text{cold}} \sim (1-100)$ pc is *far* smaller than the size of the galaxy halo, indicating a very small characteristic size for cold clouds. This is perhaps more accurately interpreted as a tiny volume filling fraction of cold gas: $f_{\text{V}} \sim N/(nR) \sim 10^{-3} - 10^{-4}$.

The observations in Table 1 span some three orders of magnitude in galaxy halo mass, along with a significant redshift range $z \sim (0.04-3.5)$. Thus, the unexpected finding that galaxy haloes are *full* of tiny, dense clouds seems to be generic. This suggests that tying the cold gas to specific star formation or feedback processes which depend sensitively on galaxy mass or redshift may be misguided; extended, cold CGM gas seems to be a nearly universal feature of galaxies. Moreover, Table 1 shows that cool CGM gas is consistently detected in quasar sightlines. Often, these can be optically thin with $N_{\text{HI}} < 10^{17} \text{ cm}^{-2}$. Specifically quantifying optically thick covering fractions (e.g. Rudie et al. 2012; Prochaska et al. 2013) therefore may not probe the physical origins of this gas. The optically thick covering fraction is known to evolve rapidly with galaxy mass (cf. Rudie et al. 2012 and Prochaska et al. 2013; Thompson et al. 2016). Faucher-Giguère et al. (2016) successfully explain these high-column-density absorbers in terms of feedback near the peak of star formation. If some cold gas is in fact always present in galaxy haloes, then radiative transfer effects may strengthen the process discussed in Faucher-Giguère et al. (2016): if cold gas in haloes is close to the self-shielding threshold, then a slight increase in the cold gas column with halo mass could lead to a large apparent increase in the optically thick covering fraction.

Absorbers start to self-shield once the neutral column $N_{\text{HI}} > N_{\text{HI}}^{\text{LLS}} \sim \sigma_{\text{HI}}^{-1} \sim 10^{17} \text{ cm}^{-2}$. Optically thin absorbers have a neutral fraction:

$$x_{\text{HI}} = \frac{an_{\text{H}}}{\Gamma} = 4 \times 10^{-3} \left(\frac{n}{10^{-2} \text{ cm}^{-3}} \right) \left(\frac{\Gamma}{10^{-12} \text{ s}^{-1}} \right)^{-1}, \quad (4)$$

where the photo-ionization rate $\Gamma \equiv 4\pi \int_{\nu_{\text{th}}}^{\infty} (J/h\nu)\sigma(\nu)d\nu$. Thus, absorbers with hydrogen column densities $N_{\text{H}} > N_{\text{HI}}^{\text{SS}} = N_{\text{HI}}^{\text{LLS}} x_{\text{HI}}^{-1} = 10^{20} n_{-2}^{-1} \Gamma_{-12} \text{ cm}^{-2}$ are capable of self-shielding. Once absorbers exceed this critical column density, they undergo a rapid transition to full neutrality beyond the photosphere. Thus, except for environments with extremely weak radiation fields, an individual isolated cloudlet $N_{\text{H}} \approx 10^{17} \text{ cm}^{-2}$ is optically thin and highly ionized. However, a cloud of droplets with $N_{\text{H}} > N_{\text{HI}}^{\text{SS}}$, or $f_{\text{A}} > 10^3 n_{-2}^{-1} \Gamma_{-12}$ will start to self-shield, rapidly approaching $N_{\text{HI}} \rightarrow N_{\text{H}}$. Note that for the purposes of continuum radiative transfer, the property of a cloud of droplets is essentially identical to that of a monolithic slab of equivalent column density. However, this

is not true for resonant line transfer, since the cloud is able to sustain large shear and turbulent velocities (see Section 4.2 for further discussion).

While there may be significant uncertainty in the photoionization modelling (particularly in the assumed flux of ionizing photons), we note that in many cases other constraints corroborate these results. In some spectra, the C II^* and Si II^* fine-structure lines, which are thought to be collisionally excited, provide an independent estimate of the electron number density within the cold gas (Prochaska & Hennawi 2009; Lau, Prochaska & Hennawi 2016); this confirms the high-volume densities leading to such small inferred cloud sizes. And in a few extraordinary cases (e.g. Rauch, Sargent & Barlow 1999), gravitationally lensed quasars directly constrain the cloud sizes in the plane of the sky to be less than ~ 30 pc; this is in excellent agreement with limits along the line of sight derived from photoionization models. Yet another constraint comes from the ‘slug nebula’ (Cantalupo et al. 2014), where the CGM is detected in fluorescent emission: the $\text{Ly}\alpha$ surface brightness ($\propto Nn$) and non-detection of He II and C IV imply a large volume density $n_{\text{H}} \gtrsim 3 \text{ cm}^{-3}$, and thus a column density $N_{\text{H}} \lesssim 10^{20} \text{ cm}^{-2}$. This corresponds to $l_{\text{cold}} \lesssim 20$ pc (Arrighi Battaia et al. 2015), again in excellent agreement with the absorption measurements in Table 1. We emphasize that these observationally derived sizes are *essentially all upper limits*: the quantity $l_{\text{cold}} \sim N_{\text{H}}/n_{\text{H}}$ gives the integrated amount of cold gas along the line of sight; this total column may come in many small steps, however, if the cold gas is in fact made up of much smaller clouds. We argue below and in Section 3.2 that this must be the case.

Currently, no explanation exists for such tiny cloud sizes in the CGM. This result becomes significantly more bizarre, however, when one considers the area covering fraction of the gas. The tiny volume-filling factors $f_{\text{V}} \lesssim 10^{-3}$ in Table 1 suggest that sightlines through galaxies should rarely intersect cold gas. However, it is rare to find sightlines *without* absorption features: Prochaska et al. (2013) find a large covering fraction (~ 100 per cent) of cold gas within the virial radius for sufficiently low-column density N_{HI} . Moreover, in cases where the cool CGM is detected in fluorescent emission (e.g. Cantalupo et al. 2014; Hennawi et al. 2015; Borisova et al. 2016; Cai et al. 2017), it visibly fills the entire halo. *Despite such tiny absorption lengths along the line of sight (and correspondingly small total mass), this cool CGM gas somehow manages to cover the entire $\gtrsim 100$ kpc extent of the halo.* In these galaxies, therefore, the area-covering fraction of cold gas vastly exceeds its volume-filling fraction $f_{\text{A}} \gg f_{\text{V}}$, indicating either that the absorption occurs in a thin shell ($\Delta R/R \lesssim 10^{-3}$) surrounding the galaxy, or that the absorption comes from a fog of tiny cloudlets distributed widely throughout the halo, as might be produced by shattering.

Since a thin shell of gas would likely not fit the fluorescent emission profiles in Cantalupo et al. (2014), Hennawi et al. (2015), Borisova et al. (2016), and Cai et al. (2017), these observations of galaxy haloes are qualitatively very suggestive of shattering: if the cold gas takes the form of a fog of tiny, distributed cloudlets, a modest total mass (or volume-filling fraction f_{V}) could naturally span the entire galaxy. As discussed in Section 1, the ratio of the two fractions is $f_{\text{A}}/f_{\text{V}} \sim R_{\text{vir}}/\ell_{\text{cloudlet}} \gtrsim 10^6$. Recall that we define f_{A} as the mean number of cloudlets along the line of sight; even if we require a large number of cloudlets ($f_{\text{A}} \gg 10^3$) to explain the smooth profiles and broad-line widths observed, shattering can easily accommodate the low volume-filling fractions $f_{\text{V}} \ll 1$ required by some observations. Whether this gas is accreted cold from the intergalactic medium (e.g. Kereš et al. 2005), stripped from satellite galaxies (Arrighi Battaia et al. 2012), forms *in situ* via thermal

⁷ This mass is left blank in a few cases where the galaxy is not detected. Absorption is such a sensitive probe of neutral gas that in some cases the observations probe the diffuse gas in the outskirts of galaxy haloes, even if the galaxy is too faint to be seen!

⁸ Inferring N_{HI} is sometimes complicated by the flatness of the curve of growth. The potentially large uncertainty and degeneracy with e.g., turbulent broadening (particularly given the large amount of turbulent broadening we now advocate) should be kept in mind.

instability (e.g. Maller & Bullock 2004; McCourt et al. 2012; Sharma et al. 2012; Voit et al. 2015), or is launched from the galaxy disc in outflows (e.g. Faucher-Giguère et al. 2016; Liang et al. 2016), we expect the gas to fragment into tiny cloudlets. These cloudlets could then disperse throughout the halo due to turbulence, producing the observed uniform covering fractions.

While these indirect arguments are extremely suggestive, they do not amount to direct observations of small-scale structure. The last group of columns in Table 1 lists the cloudlet properties predicted by shattering. The most direct comparison is to see that the total (ionization-corrected) column density of cold gas N_{H} always exceeds the minimum scale $\sim 10^{17} \text{ cm}^{-2}$ predicted by shattering. Interestingly, when the implied number of cloudlets along the line of sight $f_{\text{A}} \sim N_{\text{H}}/(10^{17} \text{ cm}^{-2})$ is large, we typically find broad-line widths, with velocities characteristic of the virial velocity of the halo. In the cases where N_{H} dips below $\lesssim 10^{18} \text{ cm}^{-2}$, the lines resolve into individual components, each with approximately thermal line widths (we denote narrow lines with a † in the first column of Table 1). This transition from broad to narrow lines around a column density of $\sim 10^{17} \text{ cm}^{-2}$ is suggestive of shattering; we discuss this further in Section 3.2.

We furthermore show that the high-volume densities and correspondingly small spatial scales of the cold gas are suggestive of shattering, though this requires assumptions about the ambient environment. Since we expect the cold clouds are pressure-confined, we define a typical hydrostatic or ‘virial’ pressure for the ambient halo gas as $P_{\text{vir}} \sim f_{\text{b}} GM^2/R_{\text{vir}}^4$. In convenient units,

$$P_{\text{vir}} \sim (2000 \text{ cm}^{-3} \text{ K}) M_{12}^{2/3} h(z)^{8/3}, \quad (5)$$

where $M_{12} \equiv M/10^{12} M_{\odot}$ is the total mass of the galaxy halo, $h(z) \equiv H(z)/H_0$ is the Hubble parameter at redshift z and we have adopted the common definition for the virial radius $R_{\text{vir}} \equiv R_{200c}$ as the radius within which the mean density is 200 times the average energy density of the universe (shown in the third column of Table 1). The baryon fraction f_{b} is uncertain in galaxies, leading to debate over the missing baryon problem; these constraints are even weaker at the redshifts $z \gtrsim 2$ relevant to quasar absorption studies. In the interest of simplicity, we adopt a cosmic baryon fraction $f_{\text{b}} = \Omega_{\text{b}}/\Omega_{\text{m}} \sim 0.17$, which probably overestimates the pressure P_{vir} in equation 5. In galaxy clusters, where the gas pressure can be measured, P_{vir} is a typical pressure within $\sim 0.1 R_{\text{vir}}$, and the pressure falls steeply at large radii (Nagai, Vikhlinin & Kravtsov 2007; Arnaud et al. 2010). We note however that the pressure profiles may be somewhat flatter, and lower in magnitude, in galaxies (see e.g. Maller & Bullock 2004 or Sharma et al. 2012; but see Fielding et al. 2017). We adopt the pressure $P_0 \equiv P_{\text{vir}}/100$ as a typical pressure between $\sim R_{\text{vir}}/2$ and $\sim R_{\text{vir}}$ (cf. Arnaud et al. 2010, their Fig. 6). Though this estimate for the pressure is quite crude, our estimates for $n_{\text{cold}} (\equiv P_0/10^4 \text{ K})$ and ℓ_{cold} (equation 1) may be easily scaled to more accurate estimates ($\propto P$ and $\propto 1/P$, respectively). Given the significant uncertainty in this gas pressure, we find remarkable agreement with the densities inferred from photoionization models: the high densities observed [$n \sim (1-10) \text{ cm}^{-3}$] are characteristic of pressure equilibrium in the haloes of these massive, high-redshift galaxies. As expected, the cloudlet size ℓ_{cloudlet} is always smaller than the observationally derived limit ℓ_{cold} often by several orders of magnitude. This implies that each sightline intercepts a large number of cloudlets (f_{A}), consistent with the broad-line widths typical of these observations.

Taken together, these results suggest a model for the CGM. When the cold CGM is visible in fluorescent emission, the

surface-brightness profiles are strongly suggestive of distributed small cloudlets, rather than a thin shell of gas. The emission profiles in Borisova et al. (2016) suggest a semi-universal mass density for the cool CGM which scales as $\sim r^{-1.5}$; this is strikingly consistent with predictions for the hydrostatic *hot* gas from some cosmological simulations (e.g. Fielding et al. 2017). However, the cold gas probed in these observations *cannot* be in hydrostatic equilibrium; balancing gravity with pressure at large radii requires gas to be near the ($\sim 10^6 \text{ K}$) virial temperature. The observations in Borisova et al. (2016) therefore suggest a dense, hydrostatic (but still invisible) CGM as is found in cosmological simulations. For reasons that remain unclear, but are possibly related to galactic winds or thermal instability, a small fraction [$\sim (1-5)$ per cent] of the CGM is cold; shattering would then imply this cold gas takes the form of tiny cloudlets interspersed throughout the hydrostatic CGM. If the small cloudlets are dynamically coupled to the hot gas (see Section 3.5, below), this could explain the hydrostatic-looking density profile for the cold gas.

A strong dynamical coupling would also imply the cold gas is long-lived (i.e., it remains suspended in the hot gas and does not fall inward), explaining why it appears in 100 per cent of the galaxies targeted by Borisova et al. (2016), even out to the virial radius. Indeed, this potentially is relevant to why cold photoionized gas is seen in absorption in both active and passive galaxies (Werk et al. 2014) – once formed, cold gas can be remarkably long-lived. If correct, this result is useful because it implies that the kinematic measurements in Borisova et al. (2016) are in fact probing the dynamics of the (invisible but dynamically dominant) hot CGM. Such kinematics seem qualitatively consistent with the cosmological simulations in Fielding et al. (2017), but we defer a detailed discussion to a later study.

To summarize, recent studies of the CGM unexpectedly find cold gas in a large fraction of sightlines through typical galaxies, at least at the redshifts $z \gtrsim 2$ most easily probed by observations. In cases where this gas can be imaged in fluorescent emission, it is indeed seen to fill the galaxy halo. Both absorption and emission observations indicate a relatively small total mass of cold gas, which is somehow present everywhere, and which follows a mass density profile consistent with $\sim r^{-1.5}$. These puzzling observations are naturally explained if the cold gas comprises a fog of distributed tiny cloudlets – in fact, the absorption and emission observations essentially *require* this interpretation. While any individual observation listed in Table 1 may have significant uncertainty, the general conclusion that at least some galaxies are filled with tiny clouds of cold, dense gas seems inescapable. More quantitatively, the lowest column-density observations in Table 1 show that the cloudlet scale we identify is consistent with available observational limits. While the origin of this cold gas is not known, the observations in Hennawi et al. (2015), Cantalupo et al. (2014), Borisova et al. (2016) and Cai et al. (2017) strongly suggest that the cloudlets are uniformly mixed with a virialized, pressure-supported CGM as is predicted in observations. We note that Stern et al. (2016) also interpret quasar-sightline observations as indicative of a large number of small clouds. This is very different from the model proposed here, however, as they consider a hierarchical model in which each absorption component corresponds to a distinct cloud, and the different components are strongly out of pressure balance. In our picture, cold gas fragments entirely to small scales and large column densities correspond to sightlines intercepting multiple cloudlets. We will make more detailed comparisons to CGM observations in a future study.

3.2 Turbulent line profiles

The observations of the cold CGM in Borisova et al. (2016) show smooth, broad emission lines. While hydrogen Ly α lines in emission can potentially be broadened by radiative transfer effects, optically thin metal absorption lines sometimes show comparable widths. The width of these emission lines can vastly exceed the $\sim 10 \text{ km s}^{-1}$ thermal width for gas at 10^4 K , indicating random motions up to $\sigma_v \sim 500\text{--}1000 \text{ km s}^{-1}$ in the cold gas (Prochaska & Hennawi 2009; Arrigoni Battaia et al. 2015; Prescott, Martin & Dey 2015; Lau, Prochaska & Hennawi 2016). If these random motions are interpreted as turbulence within the bulk of the cold gas, it corresponds to a Mach number $M \sim 100$. However, such supersonic turbulence should quickly shock on a time-scale

$$t_{\text{diss}} < 10^6 \text{ year} \times \left(\frac{\ell_{\text{out}}}{\text{kpc}} \right),$$

where ℓ_{out} is the outer scale of the turbulence (which must be below the resolution limit of the observations in order to make consistently broad-line profiles). Such shocks would heat the gas to $\sim (10^6 - 10^7) \text{ K}$, making it impossible to produce the observed line emission. This short dissipation time-scale is problematic given the relatively smooth and uniform nature of the emission profiles: if the gas is destroyed on a time-scale $\lesssim 10^6 \text{ year}$, it must somehow be continuously replenished everywhere throughout the $\gtrsim 100 \text{ kpc}$ extent of the halo. Since this time-scale is far below the cooling time of the hot gas, however, it is not clear what this uniformly distributed source of cold gas could be, or what mechanism could provide the continued turbulent stirring. Moreover, since the observations in Borisova et al. (2016) find broad lines in ~ 100 per cent of galaxies, the mechanism producing them must be present in essentially all galaxies.

Once again our proposed scenario would match the observations. Indeed, if the cold gas in the CGM represents a fog of tiny cloudlets, as discussed above in Section 3.1, the observed column densities $N_{\text{H}} \lesssim 10^{20} \text{ cm}^{-2}$ imply that sightlines intersect a large number ($\lesssim 10^3$) of cloudlets. If these cloudlets have a velocity distribution characteristic of the virial velocity of the halo, random motions among cloudlets could easily explain the observed line widths. As we discuss in Section 3.5 below, if the droplets are well dispersed and make up a small fraction of the CGM by mass, we expect they are efficiently entrained in the ambient hot medium. The broad-line widths should then reflect trans-sonic ($M \lesssim 1$) motions of the hot gas, which is typical for the turbulent motions in the virialized gas found in cosmological simulations. This picture could be readily testable in the outer parts of the galaxies, where cold gas column densities should drop: when the cold hydrogen column falls below $N_{\text{H}} \lesssim 10^{20} \text{ cm}^{-2}$, a high-resolution, high signal-to-noise spectrum of the emission line should resolve into individual sub-components with widths $\lesssim 20 \text{ km s}^{-1}$. This could be tested by, e.g. looking for an auto-correlation signal peaking at zero lag within the line spectrum. Arav et al. (1997) discuss the spectral resolution and signal to noise necessary to perform such analysis. If correct, this result is useful because it implies that the kinematic measurements in Borisova et al. (2016) are in fact probing the dynamics of the otherwise invisible hot gas. We discuss this possibility further in Section 4.2. We note that suprathermal line widths are also typical in galaxy winds (e.g. Schwartz & Martin 2004; Martin 2005), which is also consistent with shattering. However, in winds it is also possible to model broad-line widths as resulting from a large-scale velocity shear over the scale of the wind.

As we discuss in Section 3.3, the atomic gas near quasars also shows broad, smooth lines with widths corresponding to random velocities of $(10^3 - 10^4) \text{ km s}^{-1}$. Interpreting these random velocities as turbulence within the bulk of the cold gas is also problematic, but in this case for a different reason. Since the cooling time for the dense gas near quasars is far shorter than the dynamical time, this gas could easily radiate away any thermal energy deposited by shocks. However, this same mechanism should rapidly dissipate the random motions, suggesting that broad-line regions are hard to maintain and should evolve on roughly the dynamical time-scale. But broad lines are extremely characteristic of quasars and AGN, and seen in a large fraction of observations (in some cases, with an observational baseline of many dynamical times). The broad lines therefore cannot be a short-lived, transient phenomenon. Again, the problem may disappear if the cold gas takes the form of small, distributed cloudlets: the broad-line widths would then represent virial motions of the confining hot gas, as traced by a population of tiny, entrained cloudlets. The predicted number of cloudlets within BAL region and BLR is too great to test this hypothesis directly by resolving the lines into sub-components, however it may be possible in more distant absorbers such as ‘associated absorption lines’, or AALs; see Section 3.3 for more details.

In HVCs, Blagrove et al. (2017) show that the full, $\sim 100 \text{ km s}^{-1}$ velocity spread of the gas splits into features with widths of $\sim 2 \text{ km s}^{-1}$, characteristic of the thermal width for the 100 K gas probed. In both position and velocity space, they see structure all the way down to the resolvable scale. Richter (2006) and Braun & Kanekar (2005) probe the smallest scales of HVCs yet identified, with $N_{\text{HI}} \sim 10^{18} \text{ cm}^{-2}$ (and inferred sizes of a few thousand AU). Depending on the ionization fraction, these observations may approach the scale of individual cloudlets. And indeed the lines resolve into thermal widths, with resolved Lorentzian profiles.

In similar observations, but at lower temperature, Hacar & Tafalla (2011) and Hacar et al. (2013) demonstrate in a careful analysis that molecular filaments in the interstellar medium with strongly suprathermal line widths resolve into $\sim 10 \text{ s}$ of smaller sub-filaments, each with approximately thermal line widths. The relative motions of filaments sets the overall line width, and is consistent with subsonic motion of each sub-filament through the confining hot medium. While the shattering discussed in this paper does not strictly apply at temperatures far below $\sim 10^4 \text{ K}$, these results are broadly consistent with the notion that cold gas has a small characteristic scale, and that broad lines can be made by superposing a large number of narrow ones. We discuss possible extensions of shattering to the colder, 100 K gas in star-forming regions in Section 4.

3.3 Broad-lines and black holes

Here, we discuss broad atomic lines associated with black holes. In (approximate) order of increasing distance from the black hole, we discuss emission lines from the BLR, followed by absorption lines from BAL region and slightly more distant mini-BAL regions. At yet larger distances, we discuss absorbers known as FeLoBALs and AALs.

Quasars and AGNs often show broad emission lines. These lines are interpreted to come from bound gas quite close to the black hole, at a distance $\sim 0.1 \text{ pc}$ from a typical quasar. Amazingly, despite the strong radiation field so close to the AGN (e.g., a hydrogen ionizing photon flux $\Phi_{\text{ion}} \sim 10^{18.5} \text{ cm}^{-2} \text{ s}^{-1}$), and despite its orbital motion with speeds approaching $\gtrsim 0.1 c$, this gas is cold and neutral, with

a temperature $\sim 2 \times 10^4$ K (e.g. Bottorff et al. 2000). Photoionization modelling indicates a total column density $N_{\text{H}} \sim 10^{23} \text{ cm}^{-2}$ and volume density $n \sim 10^{10} \text{ cm}^{-3}$ for the line-emitting gas; the corresponding volume-filling fraction is $f_{\text{V}} \sim 10^{-6}$. Broad-line regions thus appear to comprise many small clouds which must be confined, either by ambient hot gas, or else somehow by magnetic stresses (see e.g., Rees 1987 or Netzer 2006 for reviews of broad-line regions). Despite their broad widths, the emission lines appear perfectly smooth, even in high signal-to-noise, high-resolution spectra; if they are composed of individual clouds with thermal line widths, a minimum of 10^6 – 10^8 emitters must be present within the broad-line region to explain the observed smooth line profiles (Arav et al. 1997; Dietrich et al. 1999).

Qualitatively, a large number of confined, small clouds with short cooling times seem consistent with the shattering process discussed in this paper. Shattering would produce cloudlets with a scale $\ell_{\text{cloudlet}} \sim 10^{-12}$ pc, far smaller than the observational upper limit $\ell_{\text{cold}} \sim N/n \sim 10^{-7}$ pc. While it is difficult to probe such small scales directly, this prediction that $\ell_{\text{cloudlet}} \ll \ell_{\text{cold}}$ is consistent with the need for many ($\gtrsim 10^8$) clouds in the broad-line region to explain the smooth line profiles. Radiative transfer effects are even more suggestive of tiny clouds: the column density $N_{\text{H}} \sim 10^{23} \text{ cm}^{-2}$ inferred from the ionization fraction implies gas which is too optically thick at resonant line frequencies to explain the observed spectra. Bottorff et al. (2000) show that turbulent broadening $\sigma_{\text{turb}} \gtrsim 10^3 \text{ km s}^{-1}$ is needed to lower the optical depth sufficiently to explain certain line ratios. As discussed above in Section 3.2, such large turbulent velocities seem impossible in cold dense gas. If the cold gas is a fog of small droplets confined in a virialized medium, however, such broadening can naturally be explained by virial motions of the cloudlets: even with intrinsically thermal line widths, virial motions would imply a broadening $\sigma_{\text{turb}} \sim v$, precisely as is observed. Taken together, these observational properties of BLRs – small clouds, short cooling times, low volume-filling fractions, suprathermal random motions, and unusual radiative transfer – all seem strongly suggestive of shattering.

In addition to the broad emission lines discussed above, approximately 10 percent of quasars also show BALs. When they occur, such absorption lines come from gas with a volume density $n \sim 10^{11} \text{ cm}^{-3}$, a total column $N_{\text{H}} \sim 10^{24} \text{ cm}^{-2}$ and with velocities spanning a range $\sim (0.1\text{--}0.3)c$. Elvis (2000) proposes that these clouds of cold neutral gas form in a thin, conical wind originating from the quasar accretion disc at a distance only ~ 0.01 pc from the black hole. This implies a volume-filling fraction $f_{\text{V}} \sim 10^{-4}$ of cold gas in the absorbing region. Even stronger constraints come from mini-BALs, thought to come from somewhat more distant gas with lower column density, $N \sim 10^{21} \text{ cm}^{-2}$. Photoionization modelling of mini-BAL clouds indicates a volume-filling fraction $f_{\text{V}} \lesssim 10^{-5}$, while partial obscuration of the quasar disc implies a typical area-covering fraction $f_{\text{A}} \sim 0.15$ (Hamann et al. 2013). As in the broad emission-line regions discussed above, the low-volume-filling fraction of the absorbing gas and the smooth line profiles both suggest that the region consists of a large number of small clouds, as might be produced by shattering.⁹

Absorption lines originating at larger distances from the black hole are also suggestive of shattering. Faucher-Giguère, Quataert &

Murray (2012) discuss a class of quasar absorption lines known as FeLoBALs, with lower densities ($n \sim 10^4 \text{ cm}^{-3}$), column densities ($N \sim 10^{21} \text{ cm}^{-2}$) and velocities ($v \sim 10^3 \text{ km s}^{-1}$) than the BALs discussed above. These absorption lines are interpreted to come from outflowing atomic gas at much larger distances ($\sim 1\text{--}5$ kpc) from the quasar. As in the BALs, multiple absorption components along the line of sight and smooth, suprathermal line widths both indicate the presence of many small cloudlets. Faucher-Giguère et al. (2012) show that these absorbers can be understood as the remnants of a dense molecular cloud which is overrun by the quasar shock and shredded into small cloudlets entrained in the flow. In order for this fragmentation to work, the authors suggest the initial cloud must be larger than $v_{\text{shock}} t_{\text{cool}} \sim 10 \times c_s t_{\text{cool}}$,¹⁰ where $v_{\text{shock}} \sim \text{few} \times 100 \text{ km s}^{-1}$ is the speed of the shock transmitted through the cloud. We note that the density ratio and shock speed in our simulations shown in Fig. 5 closely match some of the absorbers discussed in this paper and find a similar minimum scale for fragmenting cold gas.

At even larger distances, and correspondingly lower speeds, Finn et al. (2014) report ‘associated absorption lines’ (AALs) from a quasar spanning a factor of ~ 30 in density and temperature, seen in lines ranging from H I to Ar VII. In this case, partial covering of the quasar disc indicates an upper limit on cloud sizes $\ell \lesssim 10^{-2.5}$ pc. Photoionization modelling indicates upper limits as small as $\ell \lesssim 10^{-4.5}$ pc, depending on the temperature component probed. The lines are broad, but resolve into eight distinct velocity components, each with approximately thermal line widths. This observation is again strongly suggestive of the shattering discussed in this paper. While in most cases, we compare only to observational upper limits, the tiny size $\ell \lesssim 10^{-4.5}$ pc reported by Finn et al. (2014) is actually within a factor ~ 10 of the prediction by shattering, comparable to or better than our expected theoretical uncertainty. And the thermal line widths suggest this observation reaches a scale containing a fairly small number of cloudlets. This is the most constraining observation we have found; it is extremely demanding to explain, but appears consistent with shattering.

Table 2 summarizes these different observations of atomic gas near quasars. As in Section 3.1, we compute a total absorbing length $\ell_{\text{cold}} \equiv N/n$ and a volume-filling factor $f_{\text{V}} \equiv \ell_{\text{cold}}/R$ of cold gas. In all cases, the absorbing length ℓ_{cold} is much larger than ℓ_{cloudlet} , consistent with shattering. Moreover, the volume-filling factor is much smaller than the area-covering factor $f_{\text{A}} \sim (0.1\text{--}1)$; as discussed above, this geometry is highly suggestive of a fog-like collection of a large number of tiny clouds. The smoothness of the absorption lines also implies a large number of independent clouds, shown as $N_{\text{clouds}}^{(\text{region})}$ in the table. We compute an expected number of clouds along the line of sight $f_{\text{A}} \equiv \ell_{\text{cold}}/\ell_{\text{cloudlet}}$ using equation 1; in the case of distant absorbers such as FeLoBALs or AALs, this number may be essentially directly compared with the observational limit $N_{\text{clouds}}^{(\text{region})}$ derived from line shapes. BLRs, BALs and mini-BALs are closer to the quasar, however, and the observational limit $N_{\text{clouds}}^{(\text{region})}$ thus probes the *total* number of clouds in the system. This can be compared quantitatively with shattering theory only if we make assumptions about the geometry of the system. None the less, the

⁹ We note, however, that a large-column-density $N \gg 10^{17} \text{ cm}^{-2}$ seems inconsistent with a low covering fraction $f_{\text{A}} \lesssim 1$ in our model. In this case, the low covering fraction could represent holes in the large-scale distribution of cloudlets.

¹⁰ In their paper, this is expressed as the requirement that $t_{\text{cool}} < t_{\text{crush}}$; for a density ratio of 10^3 and a Mach number of 1.5. This is consistent with our requirement that $R \gg c_s t_{\text{cool}}$. Though these two models differ slightly in detail, they yield similar predictions for the parameters relevant to FeLoBAL absorbers.

Table 2. The neutral gas around quasars come in the form of small, dense, distributed cloudlets. In (approximate) order of increasing distance from the black hole, we list example observations of the BLR, BAL, mini-BAL, FeLoBAL and AAL regions around quasars (see Section 3.3 for definitions of the acronyms; references given in the numbered notes below the table). With the exception of the BLR, these are all seen in absorption. Though this gas is cold and neutral, it moves with extreme velocity, sometimes a significant fraction of the speed of light c . Turbulent broadening (estimated both from the width of the line, and also from radiative transfer effects influencing line ratios) indicate strongly supersonic random motions, in some cases with Mach numbers $\gtrsim 10^3$ relative to the atomic gas. As argued in Arav et al. (1997) and in Section 3.2, such broad suprathermal line widths suggest the emission comes from trans-sonic motion of cold cloudlets through the hot gas in a two-phase medium. As in the case of the CGM (Section 3.1), the area-covering fraction of cold gas is $f_A \gtrsim 1$, but photoionization modelling indicates high densities and hence a relatively small total amount of cold gas, implying volume-filling fractions as low as $f_V \sim 10^{-6}$. The last two columns in the table show the cloudlet size ℓ_{cloudlet} computed from equation 1 (which can be compared to the observational upper limit ℓ_{cold}) and the expected number of cloudlets along the line of sight f_A (which can be compared to the observational lower limit $N_{\text{clouds}}^{(\text{region})}$ based on line profiles). In all cases, the small limit for the cloud size from photoionization modelling and the large number of clouds needed to produce smooth line profiles are both consistent with the shattering process described in Section 2.

Object	Line shape		$N_{\text{clouds}}^{(\text{region})a}$	$N(\text{cm}^{-2})$	Photoionization		Shattering fragments		
	v_{outflow}	σ_{turb}/c_s			$n(\text{cm}^{-3})$	f_V	$l_{\text{cold}}(\text{pc})$	$\ell_{\text{cloudlet}}(\text{pc})$	f_A^b
<i>Nearby absorbers, $\lesssim 1\text{ pc}$ from the black hole:</i>									
BLR ^c	$(0.01 - 0.1) c$	$\gtrsim 10^{3d}$	$> 10^8$	10^{23}	10^{10}	10^{-6}	10^{-6}	10^{-12}	10^6
BAL ^e	$(0.1 - 0.3) c$	$\gtrsim 10^3$	$> 10^5$	10^{24}	10^{11}	10^{-4}	10^{-6}	10^{-13}	10^7
mini-BAL ^f	$(0.1 - 0.2) c$	$\gtrsim 10^3$	$> 10^5$	10^{21}	10^9	10^{-5}	10^{-7}	10^{-11}	10^4
<i>Distant absorbers, $\gtrsim 1 - 100\text{ kpc}$ from the black hole:</i>									
FeLoBAL ^g	$(0.003 - 0.02) c$	$\gtrsim 10^2$	—	10^{21}	10^4	—	10^{-1}	10^{-6}	10^5
AAL ^{h,i}	$\sim 0.002 c$	$\gtrsim 1$	$> 8^j$	10^{18}	10^3	$\sim k$	$10^{-4.5}$	10^{-5}	$10^{0.5}$
AAL ^l	$\sim 0.007 c$	~ 1	$> 1^j$	10^{18m}	20	—	0.02^m	10^{-3}	10^0

Notes. ^aThe number $N_{\text{clouds}}^{(\text{region})}$ here is derived from the smoothness of the line profile, assuming that the line comes from adding together many lines with intrinsically thermal widths. Since the quasar disc is not resolved, this represents the number of clouds in the entire region, not along a geometric line of sight. Also, it is strictly a lower limit.

^bHere, the number f_A is our estimate for the number of clouds along the line of sight. Since the quasar disc is not resolved, this can in principle be lower than the value $N_{\text{clouds}}^{(\text{region})}$ derived from the line shape. In practice, it seldom is.

^cRees (1987); Arav et al. (1997); Dietrich et al. (1999); Bottorff et al. (2000); Netzer (2006).

^dIn the BLR region, an additional constraint on σ_{turb} comes from radiative transfer effects (Bottorff et al. 2000).

^eElvis (2000).

^fHamann et al. (2011, 2013).

^gFaucher-Giguère et al. (2012).

^hFinn et al. (2014).

ⁱThe observation in Finn et al. (2014) contains many different components with different sizes and densities. Here, we simply quote the smallest size implied by the observation.

^jIn distant absorbers such as FeLoBALs and AALs, the observationally derived limit on the number of clouds is more like the f_A we calculate from shattering theory.

^kWe do not compute volume-filling fractions for FeLoBALs or AALs, since we have no constraints on the extent of the absorbing region. These are probably not associated with the quasar, so the distance to the quasar is not likely representative of the size of the region.

^lD’Odorico et al. (2004) (UM 680).

^mD’Odorico et al. (2004) give $N_{\text{HI}} \sim 10^{15.2}$ and $U \sim 10^{-2.3}$. We (crudely) estimated the ionization correction of $\lesssim 10^{-3}$ from Fig. 10 in Finn et al. (2014), under the assumption that similar models for the ionizing photon spectrum apply to both systems.

basic requirement of a large number of distributed clouds is easily accommodated by shattering.

Thus, atomic gas in quasar outflows appears to come in the form of small, distributed cloudlets with a low volume-filling fraction. This conclusion holds over a wide range of density, velocity and distance from the quasar, and over at least a factor of ~ 30 in temperature. Taken together, these observations are strongly suggestive of shattering.

3.4 High-velocity clouds

Galaxy surveys in 21 cm emission have found that the Milky Way halo is filled with large clouds of neutral gas. These clouds are known as either *high-velocity clouds* (HVCs) or *intermediate-velocity clouds* (IVCs), depending on their motion with respect to the local standard of rest. While HVCs and IVCs may have very different origins and dynamical histories, they appear to show

similar structure; for simplicity, we refer to both as ‘HVCs.’¹¹ HVCs show a wide range of metallicity, indicating diverse origins including the galactic fountain, stripping from the small Magellanic cloud, and accretion of pristine intergalactic gas (e.g. Richter et al. 2001; Richter 2006). Some fractions of HVCs might represent accretion from the IGM (Richter et al. 2009; Richter 2012), and may provide roughly the amount of gas needed to fuel star formation in low-redshift galaxies (e.g. Shull et al. 2009; Bauermeister et al. 2010; Genzel et al. 2010).

Since HVCs are nearby and occupy a large ($\gtrsim 5^\circ$) region on the sky, they are ideal for studying small-scale features of cold gas. Though HVCs have $\sim \text{kpc}$ spatial extents, they exhibit

¹¹ HVCs are traditionally observed in 21 cm emission, which is only possible in the Milky Way and in M31. However, Mg II and Ca II absorption studies likely probe similar gas in more distant galaxies (e.g. Ben Bekhti et al. 2008; Richter et al. 2009; Richter 2012).

structure down to scales of $\sim(10-100)$ AU (Richter, Sembach & Howk 2003). Draco is a nearby HVC which by chance lies along a relatively empty sightline at high galactic latitude through the ISM. Miville-Deschênes et al. (2017) show it has a wispy, clumpy structure down to the 0.05 pc resolution limit of their observations. They report that 50 per cent of the resolved clumps are less than two pixels across while 90 per cent are less than three pixels across; since this is a projected area, which likely consists of many overlapping cloudlets or filaments, it seems likely this result is consistent with the small-scale features being entirely unresolved. The fact that large, cold clouds such as the Draco nebula are made up of much smaller cloudlets seems consistent with shattering. However, we caution that Miville-Deschênes et al. (2017) study dust emission at ~ 100 K; shattering as described in this paper does not strictly apply to such cold gas. We discuss possible applications to gas below 10^4 K in Section 4.

HVCs are traditionally identified in 21 cm emission, which imposes the constraints $N_{\text{HI}} \gtrsim 10^{19} \text{ cm}^{-2}$ (in order to be detected in all-sky surveys) and $|v_{\text{L.O.S.}}| \gtrsim 150 \text{ km s}^{-1}$ (in order to stand out from neutral gas in the Milky Way disc). As is the case in the CGM, absorption studies of HVCs are more sensitive to small structures and low-column densities than emission studies. Braun & Kanekar (2005) and Richter, Westmeier & Brüns (2005) study Ca II absorption and 21 cm absorption towards bright quasars in the vicinity of HVCs, probing lower column-density gas than can be seen in 21 cm all-sky surveys. They report tiny ($\sim 10^{-2}$ pc) clouds with column densities $N_{\text{HI}} \sim (0.4-8) \times 10^{18} \text{ cm}^{-2}$, pressures $\sim 10^3 \text{ cm}^{-3} \text{ K}$, and thermal line widths, in excellent agreement with shattering. This is in the limit where each sightline passes through only a few cloudlets, as might be expected near the periphery of HVCs (Ben Bekhti et al. 2008, 2009). As in the high-redshift CGM, these observations find a high covering fraction along with a tiny absorbing length of cold gas, suggesting a population of tiny, distributed cloudlets. Moreover, the narrow line widths and multiple absorbing components along the line of sight suggest dense, small, clumpy structures rather than diffuse, extended clouds. This is confirmed by the deep 21 cm emission image in Braun & Kanekar (2005).

Richter et al. (2009) present UV spectroscopy towards bright quasars and identify a sample of even lower column density HVC absorbers. The two¹² smallest clouds they identify have ionization-corrected column densities $N_{\text{H}} \sim 10^{17.2} \text{ cm}^{-2}$, consistent with single clouds produced by shattering. These sightlines also show narrow line widths, $\lesssim 10 \text{ km s}^{-1}$, as would be expected for emission from a single cloudlet. These absorption observations suggest that low-column density clouds are extremely common, even in the most tenuous parts of the Milky Way halo. The lowest column densities probed are consistent with predictions from shattering, over a fairly wide range in ionization state (and thus in the observable column N_{HI}).

As mentioned above, HVCs are classically defined to have column densities $N_{\text{HI}} \sim 10^{19} \text{ cm}^{-2}$ and velocities $|v_{\text{L.O.S.}}| \gtrsim 150 \text{ km s}^{-1}$. Ben Bekhti et al. (2008, 2009, 2012) suggest that HVCs represent only the high-column-density tail of a wide distribution of high-velocity gas. By comparison with high-redshift studies of the CGM, we furthermore suggest the Milky Way CGM shows a wide range in velocity, with most of the gas falling far below the threshold to be considered an HVC. The low-column density $N_{\text{H}} \sim 10^{17} \text{ cm}^{-2}$ and area-covering fraction $f_{\text{A}} \gtrsim 20$ per cent compared to the

high-redshift CGM observations discussed in Section 3.1 likely reflect the velocity cut ($\gtrsim 150 \text{ km s}^{-1}$) for material to be considered an HVC. This would indicate that only a small fraction of the Milky Way's CGM lies above this threshold, as seems reasonable (Zheng et al. 2015), and explains why the cold ($T < 10^6 \text{ K}$) mass of the Milky Way's CGM appears 1–2 orders of magnitude less than other L_* spirals (Stocke et al. 2013; Werk et al. 2014), where this velocity cut is not applied.

3.5 Entrainment in multiphase galactic winds

Galactic winds are a common feature of rapidly star-forming galaxies. These winds play an important role in galaxy formation: not only do they influence both the baryon budget and the star formation rate in galaxies, but galactic winds also control the chemical evolution of the intergalactic medium. One striking feature of galactic winds is the presence of multiphase gas spanning a wide range of density and temperature: molecular, atomic and X-ray emitting gas are all detected, often moving at similar velocity (see section 1 of Zhang et al. 2017 for a summary of the available observations).

Such comoving multiphase gas is difficult to understand theoretically, because the acceleration time-scale for drag forces to make different gas phases co-move:

$$t_{\text{acc}} \sim \left(\frac{\rho_{\text{cloud}}}{\rho_{\text{hot}}} \right) \frac{R_{\text{cloud}}}{v_{\text{rel}}}, \quad (6a)$$

is much longer than the time-scale to destroy the cooler phase:

$$t_{\text{crush}} \sim \left(\frac{\rho_{\text{cloud}}}{\rho_{\text{hot}}} \right)^{1/2} \frac{R_{\text{cloud}}}{v_{\text{rel}}}, \quad (6b)$$

by either shock-heating (i.e. ‘crushing’), or hydro instabilities such as the Kelvin–Helmholtz or Rayleigh–Taylor instabilities (e.g. Klein et al. 1994; Mac Low et al. 1994). The ratio between these two time-scales, $\sim(\rho_{\text{cloud}}/\rho_{\text{hot}})^{1/2}$, can be very large in strongly multiphase gas as observed in galaxy winds, suggesting that we should a priori not expect multiphase gas to co-move (see Zhang et al. 2017 and Brüggén & Scannapieco 2016 for a detailed analysis of this problem).

Some studies have identified mechanisms to delay the disruption of gas clouds, possibly enabling entrainment over a range of parameters (e.g. Cooper et al. 2009; McCourt et al. 2015). However, the entrainment problem is significantly exacerbated by the observation that cold gas is not only accelerated before it is destroyed, but also accelerated to very high velocity ($> 1000 \text{ km s}^{-1}$ in some cases) even at small distances, close to the wind launching region. These observations suggest that the acceleration time-scale is in fact much shorter than the crushing time-scale: $t_{\text{acc}} \ll t_{\text{crush}}$.

One possible explanation is that the cold gas arises from thermal instability in the hot wind, and thus could be born comoving with the hot gas (e.g. Martin et al. 2015; Thompson et al. 2016), although this possibility has not yet been verified in numerical simulations. Regardless of its origin, however, shattering substantially modifies the dynamics of cold gas clouds and may imply near-instantaneous entrainment. As an initially monolithic cloud travels through a hot medium, it shatters into tiny cloudlets with a size $\ell_{\text{cloudlet}} \sim c_s t_{\text{cool}} \sim (0.1 \text{ pc})/n$ (equation 1). The simulations in Figs 5 and 6 suggest this fragmentation enables rapid entrainment of cold gas. While the system of cloudlets as a whole may move rapidly, the interstitial hot gas between the droplets shows little random motion with respect to the cloud centre of mass. This implies little velocity shear on the scale of the cloudlets to shred them and

¹² We suspect a typo in their reported numbers for RXJ 1230.0+0115 in table 4. We therefore do not consider this sightline here.

mix the gas phases. However, these results must be confirmed in a more detailed, 3D study, probably including magnetic fields.

From a macroscopic perspective, the ‘entrainment in trouble’ problem comes from taking the ratio of equations 6a and 6b, which are appropriate for single clouds embedded in an otherwise undisturbed flow. Shattering the cloud into tiny cloudlets vastly decreases the column density through the cloud material, thereby increasing the surface-area-to-mass ratio, like the unfurling of a parachute. This not only helps explain the puzzling QSO sightline observations, in which a small total amount of cold gas manages to cover a vast region of space, but also dramatically amplifies the drag force on the cold gas, closely coupling the dynamics of the hot and cold phases.

Implicit in this discussion is the assumption that cold gas mass is conserved, i.e., that little or no mixing takes place. Testing this hypothesis will require significantly more detailed work. However, we note that, in all of the observations we mentioned, cold gas appears to be stable, ubiquitous, and long-lived, even on small scales. We do not find any compelling observational evidence for mixing between the gas phases, or for conductive evaporation of cold gas. Radiative cooling is already known to strongly suppress the small-scale mixing due to the Kelvin–Helmholtz instability (Mellema, Kurk & Röttgering 2002; Cooper et al. 2009), and this effect becomes progressively stronger with increasing numerical resolution, ultimately resulting in the shattering discussed in this paper. We note that uncontrolled numeric instabilities likely overestimate mixing in our simulations, perhaps significantly (Appendix B and Lecoanet et al. 2016). We suspect that once the cooling length $c_s t_{\text{cool}}$ is resolved and numeric instabilities are controlled, simulations will find that mixing is strongly inhibited.

4 DISCUSSION

As we discuss in Appendix B, hydrosimulations of multiphase gas may be prone to a number of poorly understood errors. More direct constraints may therefore come from laboratory experiments. Suzuki-Vidal et al. (2015) study the bow shock generated by the collision of two counter-streaming supersonic plasma jets, meant to mimic bow shocks due to jets in young stellar objects. While the plasma cooling function in these experiments is quite different from astrophysical plasmas, it none the less contains a peak, and the authors find behaviour consistent with shattering: the initially smooth bow shock fragments via thermal instability into small-scale clumps of order $\sim c_s t_{\text{cool}}$. Such laboratory experiments are a potential way of calibrating and corroborating numerical calculations of strongly multiphase gas.

In the remainder of this section, we discuss theoretical uncertainties in our work, which must be addressed in a future study (Section 4.1), along with promising directions for future research (Section 4.2). We discuss numerical uncertainties in Appendix B.

4.1 Theoretical uncertainties

In this paper we have made a number of significant assumptions and idealizations, whose effects should be explored in future work. We list several below.

Applicability of hydrodynamics. The mean-free path of charged particles due to Coulomb collisions is roughly independent of their mass. For the conditions relevant to the CGM, we find a collisional mean-free path $\lambda_{\text{mfp}}^{(\text{hot})} \sim 3$ pc, which is much larger than the expected

size of cloudlets we consider. We can quantify the collisionality via the Knudsen number:

$$\sigma \equiv \frac{\lambda_{\text{mfp}}^{(\text{hot})}}{\ell_{\text{cloudlet}}} \sim 300 \times \left(\frac{T}{10^6 \text{ K}} \right)^2, \quad (7)$$

where we have assumed thermal pressure balance between the hot and cold phases. This large disparity calls into question where hydrodynamics is at all applicable at the cloudlet scale.¹³ Since particles cannot effectively exchange momentum on such small scales, one might expect that pressure confinement is impossible and that the cold cloudlets would simply disperse.¹⁴

One possible conclusion is that clouds only shatter down to scales of order the mean-free path. However, even a weak magnetic field significantly influences particle motion in dilute plasmas and the mean-free path in equation 7 is not likely representative if magnetic fields drape around the cloudlets. It may be that a fully kinetic calculation is necessary, but in this paper, we have simply assumed that standard hydrodynamics/MHD still applies. This assumption must ultimately be tested by PIC simulations; however, several arguments suggest the possible validity of a fluid approach: (i) Magnetic fields. In the cross-field direction, the characteristic scale is the gyro-radius $r_L \ll \ell_{\text{cloudlet}}$. Swept-up magnetic fields draped across a cloudlet enable a contact discontinuity to be maintained, as observed in galaxy cluster ‘cold fronts’ (Markevitch & Vikhlinin 2007). (ii) Plasma instabilities. Halo gas at cloudlet scales is similar to the solar wind: a $\beta \sim 1$, weakly collisional plasma, where plasma instabilities such as the firehose and mirror instability, which feed off pressure anisotropies, provide an effective scattering mechanism and can reduce the particle mean-free paths to orders of magnitude below their Coulomb value (Sharma et al. 2006; Bale et al. 2009; Kunz, Schekochihin & Stone 2014). The collisionless shocks observed in galaxy clusters provide another example of regions where density discontinuities are maintained by collisionless processes. (iii) Galaxy clusters. The mean-free path in galaxy clusters is $\lambda_{\text{mfp}} \sim 20$ kpc, which is comparable to the size of cluster cores. Yet clusters are routinely modelled with MHD, producing results which closely match X-ray observations. We also note that cold gas filaments are sometimes observed in cluster cores with scales far below the Coulomb mean-free path. (iv) Finally, perhaps the best argument is the observational evidence, both direct and indirect, in very different environments, for small-scale structure in cold gas. These observations may in turn represent an opportunity to learn and constrain plasma processes on these collisionless scales.

Thermal conduction. Thermal conduction erases small-scale temperature structure and, since the hot gas is collisionless on the expected scale of the cloudlets, we might expect they are subject to a very large conductive heat flux. Cowie & McKee (1977) identify three regimes based on the saturation parameter $\sigma'_0 \equiv 1.84 \times \lambda_{\text{mfp}}^{(\text{hot})} / \ell_{\text{cloudlet}}$: (i) classical diffusive conduction, with $\sigma'_0 < 1$; (ii) saturated conduction, with $1 < \sigma'_0 < 100$, in which the heat flux saturates at $Q \sim 5Pc_s$ since energy cannot be transported at a rate significantly larger than the electron thermal velocity; and (iii) a two-fluid regime with $\sigma'_0 > 100$, in which hot gas particles freely penetrate the cloud (Balbus & McKee 1982). From equation 7, we are either in regimes (ii) or (more often) (iii). In regime (ii), the

¹³ Note that the fluid approximation is certainly valid in the cold gas, where $\sigma \ll 1$. It is only invalid in the tenuous hot gas on cloudlet scales.

¹⁴ If pressure confinement were not an issue, this large mean-free path implies a very low Reynolds number for droplet dynamics.

heating time-scale

$$t_{\text{heat}} \sim \frac{PV}{Q \times 4\pi R^2} \sim \frac{1}{15} \left(\frac{c_s^{(\text{cold})}}{c_s^{(\text{hot})}} \right) t_{\text{cool}} \ll t_{\text{cool}}, \quad (8a)$$

which implies rapid evaporation. In regime (iii), hot electrons freely permeate the cold gas (leaving aside thorny questions of confinement and plasma instabilities). The Coulomb heating rate is $\Gamma = (5.5 \times 10^{-14} \text{ erg/s/cm}^3) n_{\text{hot}} T_{\text{hot}}^{-1/2}$ (Schunk & Hays 1971). If we compare this to the cooling rate, we obtain:

$$t_{\text{heat}} = (10^{-2} t_{\text{cool}}) \times \left(\frac{T_{\text{hot}}}{10^7 \text{ K}} \right)^{3/2} \ll t_{\text{cool}}, \quad (8b)$$

where we have assumed pressure balance. This also implies rapid evaporation. Thus, in principle whenever hot gas directly abuts cold gas without a thermal conduction front, the cloudlets are evaporated.

3D simulations of cold clouds in galactic winds with classical, diffusive thermal conduction also conclude that either thermal conduction must be suppressed, or the cold clouds seen in outflows do not originate from the galaxy (Brüggen & Scannapieco 2016). In particular, low-column density clouds $N_{\text{H}} < (10^{18} \text{ cm}^{-2}) (T/10^7 \text{ K})^2$ evaporate and disrupt rapidly.

In this paper, we assume that thermal conduction is suppressed, by either magnetic fields or plasma instabilities. We believe this is well-motivated. Conduction is essentially observationally unconstrained; to our knowledge, there is no *direct* evidence for thermal conduction in the ISM. The only environment where *Spitzer* heat fluxes have been directly measured is in the solar wind, which is defined by a large-scale, ordered magnetic field (Bale et al. 2013). Even in the hot intra-cluster medium (ICM), where conduction might be expected to be extremely effective, there is no compelling observational evidence for conduction (e.g., broad conductive interfaces, though note Sparks et al. 2009), and the literature contains a number of assumptions ranging from complete suppression to fully *Spitzer* values. Interestingly, simulations of magnetic draping along cold fronts suggest that significant suppression of conduction along field lines is still required to explain the observed sharpness of fronts (ZuHone et al. 2013), as magnetic insulation always has some imperfections. The required reduction could potentially come from small-scale plasma instabilities which scatter particles and reduce the mean-free path (Komarov et al. 2016).

With regard to our specific applications to the CGM, it is worth noting that even if we abandon our droplet model and adopt the conventional monolithic absorber model in which a single cloud of size $l_{\text{cold}} \sim N/n$ accounts for the observed absorption, conduction *still* must be suppressed in order to explain these observational upper limits: (i) in Table 1, for the $z \sim 2$ systems *a–d*, for instance, $l_{\text{cold}} \sim 20 \text{ pc} \ll \lambda_{\text{mfp}}^{(\text{hot})} \sim (250 \text{ pc}) T_7^2 n_{-3}^{-1}$, while the Field length $\lambda_F^{(\text{hot})} \sim (80 \text{ kpc}) T_7^2 n_{-3}^{-1/2}$. If there is no conductive interface, and we adopt the saturated conduction rate, the cloud will be destroyed on a hot gas sound-crossing time: $t_{\text{heat}} \sim R/c_s^{(\text{hot})} \sim 2 \times 10^4 \text{ year}$. (ii) Even in stable or condensing scenarios, where radiative losses can outstrip conductive heat supply, thermal contact must be sufficiently poor that conduction only supplies a small fraction of radiated energy. Otherwise, the cold gas would rapidly cool the hot gas, leading to a massive cooling flow. Given that $L \propto \int n^2 \Lambda(T) dV \propto M n \Lambda(T)$, the radiative cooling rate in cold gas can be significantly higher than in the hot gas:

$$\frac{L_{\text{cold}}}{L_{\text{hot}}} \sim \frac{n_{\text{cold}} M_{\text{cold}} \Lambda(T_{\text{cold}})}{n_{\text{hot}} M_{\text{hot}} \Lambda(T_{\text{hot}})} \sim 100 \left(\frac{\delta}{10^3} \right) \left(\frac{f_{\text{M}}}{10^{-2}} \right) \left(\frac{\Lambda(T_{\text{cold}})/\Lambda(T_{\text{hot}})}{10} \right) \quad (9)$$

where $\delta \equiv n_{\text{cold}}/n_{\text{hot}} \sim T_{\text{hot}}/T_{\text{cold}}$ is the density contrast, and f_{M} is the cold gas mass fraction. This results in a cooling time for the hot gas of:

$$t_{\text{cool}}^{(\text{hot})} \sim \frac{M_{\text{hot}} k T_{\text{hot}}}{n_{\text{cold}} M_{\text{cold}} \Lambda(T_{\text{cold}})} = \frac{\delta}{f_{\text{M}}} t_{\text{cool}}^{(\text{cold})} \sim (5 \times 10^7 \text{ year}) \times \left(\frac{\delta}{10^3} \right) \left(\frac{f_{\text{M}}}{10^{-2}} \right)^{-1}, \quad (10)$$

which would cause a complete collapse of the hot hydrostatic atmosphere. This implies that we require $t_{\text{conduct}} \gg t_{\text{cool}}$ in the cold gas and strongly argues against scenarios where cold clouds are continuously evaporated and reformed: they are too efficient as coolants of the hot gas. Since the Ly α luminosity is comparable to the X-ray luminosity of low-redshift clusters, this is similar to the cooling flow problem there, which is generally resolved by heat input into the hot phase (e.g., by AGN). Having cold clouds as a coolant is especially pernicious, however, since it produces a cooling flow problem in regions which otherwise have a long cooling time (e.g., the outskirts of galaxy clusters) and where heating is not expected to be effective. Since we directly observe the cold gas in absorption, we interpret this as strong evidence that thermal conduction is suppressed, at least at the interface between cold and hot gas.

Effect of magnetic fields. As already discussed, magnetic fields affect diffusion transport coefficients such as conduction and viscosity. The effects of magnetic pressure and tension can also alter the dynamics of shattering. In the preliminary work, we have found that thermal instability in a stratified medium is *enhanced* by magnetic tension, since tension suppresses the internal gravity waves which quench instability (Ji, Oh & McCourt 2017). In principle, magnetic pressure could inhibit shattering, if the cold phase is magnetically rather than thermally supported. In an extreme case, where the plasma $\beta \ll 1$, isochoric cooling without shattering might be feasible. In practice, we expect magnetic fields to introduce anisotropy into the shattering process. Note that in the ISM, the magnetic field strength appears to be independent of temperature or phase for $n \leq 300 \text{ cm}^{-3}$ (Crutcher et al. 2010), which is potentially explicable by reconnection diffusion (Lazarian 2014). Non-thermal pressure support appears to be important primarily in much denser gas, which is self-gravitating.

Photoionization. We have assumed cooling functions appropriate for gas in collisional ionization (coronal) equilibrium. However, ISM/CGM gas is illuminated by both the local galactic radiation field and the metagalactic UV/X-ray background – indeed, most of the studies that motivated our work used photoionization models to estimate the physical properties of the gas. Both photo-heating and photoionization of important atomic coolants can significantly change cooling efficiencies as a function of temperature (Wiersma, Schaye & Smith 2009; Cantalupo 2010; Gnedin & Hollon 2012; Kannan et al. 2014). For typical radiation fields, with gas at low density ($n \sim 10^{-3} \text{ cm}^{-3}$) and optically thin to H/He photoionizing radiation, the effect is modest at $T > 10^5 \text{ K}$ (when metal line cooling prevails), but leads to a drastic reduction of cooling below $T \sim 10^5 \text{ K}$ and, depending on the hardness and strength of the radiation field, an elevated equilibrium temperature $10^4 \text{ K} < T < 10^5 \text{ K}$. Thus, it is unlikely to be important in high-redshift absorption systems (e.g., items *b–e* in Table 1), which are much denser ($n \sim 1 \text{ cm}^{-3}$) and self-shielding ($N_{\text{HI}} > 10^{17} \text{ cm}^{-2}$), with inferred neutral fractions from photoionization modelling $x_{\text{HI}} \sim 0.1–1$. However, these effects are potentially important in the emitting gas in the Slug nebula

(Arrighi Battaia et al. 2015) and the jackpot nebula (Hennawi et al. 2015), and in low-redshift systems (Stocke et al. 2013; Werk et al. 2014), which have much lower densities and are optically thin to H/He ionizing radiation. Naively, if we assume shattering halts at $T \sim 10^5$ K, then from the red curves in Fig. 2, there would only be an order of magnitude increase in N_{cloudlet} . However, the dynamics of shattering may change, given a reduced temperature contrast between ambient and cool gas. These considerations may also be important for the abundance of O VI absorbers (since the collisional ionization abundance of O VI peaks at $T \sim 2 \times 10^5$ K).

Relevance to low- z haloes. Both magnetic fields and photoionization are potentially relevant to the qualitatively distinct features inferred in low-redshift CGM by Werk et al. (2014). In particular, Werk et al. (2014) report very low densities for the cold gas in low-redshift galaxies (comparable to the expected density for the hot gas), along with high-column densities of cold gas, $N_{\text{H}} \sim 10^{20} \text{ cm}^{-2}$. The large volume filling factor implied by this low density is more consistent with a single, monolithic absorber than with a fog of cloudlets. However, these inferences are more model-dependent than high- z observations:¹⁵ unlike the latter, the low-redshift absorbers are optically thin and highly photoionized, with a large (and uncertain) photoionization correction ($x_{\text{HI}} \sim 10^{-3.5}$, compared to $x_{\text{HI}} \sim 0.1 - 1$ at high redshift). This leads to sensitivity to the assumed ionizing spectrum, as well as the assumption of a single temperature and density for all absorption lines. Models which allow for a range of densities obtain qualitatively different results (Stern et al. 2016). Moreover, assuming pure photoionization with all gas at $T = 10^4$ K ignores higher temperature collisionally ionized gas. Cosmological simulations which can account for this would report artificially low gas densities if pure photoionization is assumed (A. Kravtsov, private communication). None the less, if these low reported densities and large cloud sizes continue to be found, this potentially points towards different cooling or shattering dynamics in the CGM of low-redshift galaxies, potentially due to non-thermal pressure support (such Wiener, Oh & Zweibe 2017) or photoionization effects.

Another low-redshift observation which seems inconsistent with our model is the study of absorption sightlines through the Virgo cluster in Yoon et al. (2012). While these authors find a large covering fraction of neutral hydrogen, the column densities ($N_{\text{HI}} \sim 10^{13} \text{ cm}^{-2}$) are very low compared to the column $N_{\text{cloudlet}} \sim 10^{17} \text{ cm}^{-2}$, we expect through a single cloudlet.

Collisions and coagulation. While we have identified a characteristic scale for cold gas, not all the cold gas necessarily shatters down to this scale. For instance, the Jeans mass implies a characteristic scale for fragmentation, but collisions and coagulation allow for a broad (power-law) range of masses which cuts off at the Jeans mass (Bonnell, Bate & Vine 2003). The coagulation process also depends on non-thermal components such as magnetic fields, turbulence and details of turbulent dissipation and mixing between hot and cold phases. These are prone to artificial coagulation if under-resolved (see the third panel in Fig. 4 and discussion in the text) and demand detailed 3D simulations, which are beyond the scope of this paper.

Cooling below 10^4 K. In this paper, we have considered only a two-phase medium, with $T \sim 10^4$ K gas and a significantly hotter phase. We have not explored whether there could be shattering in even colder gas, which cools via atomic fine structure lines, molecular, or dust cooling. We conjecture (but do not show) that pressure confined gas shatters down to the *minimum* in the parameter $c_s t_{\text{cool}}$. Since this minimum generally lies at $T \sim 10^4$ K, this would imply that gas cooling to much lower temperatures would not shatter any further but remain at the scale ℓ_{cloudlet} we have identified. In other words, below $T \sim 10^4$ K, clouds cool isobarically and always remain in sonic contact with their surroundings. Note, however, that cold molecular gas tends to be self-gravitating and highly supersonically turbulent, so the governing dynamics change dramatically.

4.2 Implications and directions for future work

Since multiphase gas is ubiquitous in astrophysics, and we expect shattering to occur whenever the cold phase is pressure confined, the work presented here may have broad applications. We list a few possibilities here.

Turbulence in galaxy and cluster haloes. Even weak turbulence in the hot hydrostatic atmospheres of galaxy clusters can have an outsized impact on their evolution: turbulence advects metals and entropy, affects the topology and (via the turbulent dynamo) strength of magnetic fields and thus influences the diffusion coefficients such as thermal conduction and viscosity. At larger amplitudes, turbulence might be an important source of pressure support, influencing both the evolution of galaxy clusters and their utility for constraining dark energy. Thus, directly measuring turbulent line broadening in clusters was an important goal for Hitomi, which unfortunately in its brief lifetime was able to make only a single measurement, finding a turbulent energy density $U_{\text{turb}} \sim 4$ per cent U_{therm} in the core of the Perseus cluster (Hitomi Collaboration et al. 2016).

If shattering enables the rapid entrainment of cold gas as we suggest in Sections 2.2 and 3.1, cold gas may directly reflect the kinematics of its surrounding hot gas. Indeed, this is our interpretation of the broad hydrogen Ly α line widths seen at high redshift (Hennawi et al. 2015; Borisova et al. 2016). This would imply that Keck spectroscopy of cold gas in clusters could measure ICM turbulence with much higher signal to noise and spectral resolution than was possible with Hitomi.¹⁶ Moreover, Hitomi only had the surface brightness sensitivity to observe a small handful of nearby clusters, largely in their cores. By contrast, even if the Ly α surface brightness is too faint to image in nearby clusters, absorption-line spectroscopy towards background quasars could still be performed for a large number of systems. Unlike emission-line observations, this sensitive probe extends to high redshift, to lower mass systems and out to the virial radius (as the Hennawi et al. 2015 observations make clear). At high spectral resolution, the details of the line shape can yield rich information about turbulence, such as its volume-filling factor and the importance of bulk motion (Shang & Oh 2012). If cold CGM gas such as that found in Hennawi et al. (2015) in fact persists in low-redshift clusters, then targeted spectroscopy of background quasars behind galaxy clusters could yield rich dividends.

¹⁵ Or BAL observations, where extremely high densities imply low ionization parameters and high neutral fractions.

¹⁶ Hitomi instrumental resolution was comparable to the expected turbulent broadening ($\sim 150 \text{ km s}^{-1}$), whereas optical/UV spectroscopy has an order of magnitude higher resolution.

UV escape fractions from low-mass galaxies. Shattering vastly increases surface area to volume for neutral gas, implying that the area covering fraction f_A may be large, even when the mass fraction of cold gas is negligible. For a fixed column density of neutral gas, this effectively increases the optical depth and suggests that the escape fraction of ionizing photons f_{esc} could be very small due to a fog of obscuring cold gas which envelops the entire halo. The escape fraction f_{esc} is perhaps the most uncertain and hotly debated parameter in models of reionization, with few available empirical constraints (e.g., Siana et al. 2010). In our model, the escape fraction is likely to *increase* in lower mass haloes (which are critical for reionization) for three reasons: (i) below $\sim 10^{11} M_\odot$, galaxy haloes may lose the hydrostatic atmospheres in which droplets can remain suspended (Birnbom & Dekel 2003; Kereš et al. 2005; Fielding et al. 2017); (ii) even if halo gas persists in haloes less massive than $\sim 10^{11} M_\odot$ (e.g., due to heating processes or galactic winds), the reduced temperature contrast between a lower virial temperature and the $\sim 10^4$ K cold phase may inhibit shattering; and (iii) the reduced column density of gas in smaller haloes could also mean that cold gas is no longer self-shielding to the external UV background.¹⁷ Observationally, comparing the emissivity inferred from the Ly α forest and UV luminosity functions implies that the escape fraction must increase with redshift (Kuhlen & Faucher-Giguère 2012; Becker & Bolton 2013), which could be linked to tentative evidence that f_{esc} increases at lower UV luminosity (Dijkstra, Gronke & Venkatesan 2016).

This fog of cold gas also has crucial effects on radiative transfer of resonant line photons, most notably Ly α . Each of the cloudlets is still optically thick to Ly α ($N_{\text{H I}} > 10^{14} \text{ cm}^{-2}$ for typical ionization corrections, particularly once shadowing and mutual shielding from the radiation field is taken into account). Radiative transfer in a multiphase medium, with scattering off numerous optically thick clouds (Neufeld 1991; Hansen & Oh 2006), has distinct and unique properties. The line profile, escape fraction in the presence of dust, etc., all change considerably. Moreover, a fog of cloudlets has orders of magnitude more scattering clouds than have been considered in theoretical studies to date. As previously discussed, due to their entrainment within the hot gas, these cloudlets may sustain large relative velocities. In this scenario, the mean-free path of Ly α photons could be comparable to the correlation length of the velocity field, invalidating the common assumption of micro-turbulent broadening (i.e., by adopting a turbulent b -parameter). Detailed comparison of Ly α radiative transfer calculations to observations could sharpen and test our models for cold gas. An even more extreme environment where all these effects would be taking place is the broad-line region around quasars (Section 3.3).

Cosmological simulations. Our results have important consequences for cosmological simulations. While zoom-in simulations achieve high ($\sim \text{pc}$) resolution in star-forming regions, the effective Lagrangian nature of AMR or SPH codes implies comparatively poor resolution ($\sim \text{kpc}$) in galaxy haloes. It is currently infeasible to resolve shattering in cosmological simulations, and this failure

may result in artificial mixing and destruction of cold gas.¹⁸ Instead, we advocate that cold gas should be modelled in a sub-grid fashion similar to how stars are modelled, with source and sink terms, and with a drag force coupling it to the hot phase. We plan to develop and test such an implementation in the future.

Small coherence scale in low-column absorbers. A prediction of our model is that the coherence scale of low-column density absorbers ($N_{\text{H I}} < 10^{18} \text{ cm}^{-2}$) should be undetectably small for absorption line measurements along multiple sightlines to lensed quasars. Alternatively, in the Milky Way, the very small size of a low-column density cloudlet could potentially be constrained by proper motion: the absorption signature against a background quasar could disappear on approximately decade long time-scales. This could also be tested using time variability of absorption lines in quasar spectra, both from local absorbers (e.g. Hamann et al. 1995) and from absorption by intervening galaxies (e.g. Hacker et al. 2013).

5 SUMMARY

As discussed in Section 1, several observational properties seem to be typical of cold (10^4 K) gas in astrophysics, while at the same time very difficult to explain. These include broad absorption and emission lines, large area-covering fractions relative to the volume-filling fraction, and comoving hot and cold phases; in most cases, *none* of these observations are predicted by current theoretical models of cold gas. In this paper, we suggest that such apparent inconsistencies stem from an implicit assumption that cold gas in astrophysics comes in the form of contiguous, monolithic ‘clouds.’ We suggest that many observations are naturally explained if cold gas instead takes the form of tiny cloudlets, distributed sparsely throughout space in a manner analogous to a mist or a fog. In this sense, we suggest that astrophysical ‘clouds’ have a similar form to actual, meteorological, *clouds*.

In Section 2.1 (cf. Voit & Donahue 1990), we describe a hydrodynamic process which quickly fragments cold gas to tiny scales and may produce a fog-like collection of small, distributed cloudlets as implied by observations. This process, which we call ‘shattering’, is closely analogous to fragmentation by the Jeans instability, but with contraction driven by cooling and compression by ambient pressure instead of by self-gravity. We expect cold gas to fragment down to the lengthscale $c_s t_{\text{cool}} \sim 0.1 \text{ pc}/n$, where n is the volume density in cm^{-3} , such that individual cloudlets have a characteristic column density $N_{\text{cloudlet}} \sim 10^{17} \text{ cm}^{-2}$, relatively independent of their environment. Interestingly, this column density implies that, under a wide range of conditions, individual cloudlets are (depending on ionization corrections) either optically thin or at most marginally optically thick to continuum radiation, but optically thick to resonant lines. We motivate the scale $c_s t_{\text{cool}}$ in Section 2.1, we demonstrate fragmentation to this characteristic scale in simulations in Section 2.2 and in Fig. 5, we compare our results to recent laboratory experiments in Section 4, and we discuss connections to the previous work in Appendix B. Our simulations and calculations none the less contain significant uncertainty; we discuss the most relevant shortcomings in Appendix B and in Section 4.1. We therefore rely heavily on observational data for interpreting and corroborating our model.

¹⁷ There appears to be tentative evidence for such a sharp transition in the covering fraction of optically thick gas around quasar haloes (Prochaska et al. 2013) ($f_{\text{cov}} \sim 65$ per cent) compared to that around Lyman break galaxies (Rudie et al. 2012) ($f_{\text{cov}} \sim 30$ per cent) at $z \sim 2$ –2.5, over a factor of only ~ 3 in typical halo mass.

¹⁸ Interestingly, the poor mixing seen in ‘old’ SPH or low-resolution codes may in fact be a more accurate representation of the two gas phases.

We compare our results to astrophysical observations of cold gas in Section 3, finding evidence for shattering in the CGM in galaxy haloes (Section 3.1), in the broad-line widths frequently observed (Section 3.2), in quasar spectra (Section 3.3), in HVCs (Section 3.4), and in galactic winds (Section 3.5). In these cases, the small characteristic lengthscale implied by shattering may explain observational features which are otherwise very difficult to understand. Our comparison with observations is necessarily incomplete, but suggests how shattering may be tested quantitatively in the future with more detailed studies.

In this paper, we are intentionally agnostic about the *origin* of cold gas, and thus cannot specify the amount of cold gas present in any particular environment; we simply show that shattering is inevitable once it forms. In galactic haloes, perhaps the two most likely sources of gas are thermal instability and galactic winds. Another source of cold gas may be cold streams accreting from the cosmic web. An analysis of the adiabatic case indicates they may be unstable to the Kelvin–Helmholtz instability (Mandelker et al. 2016). These streams would likely shatter in the presence of radiative cooling, perhaps explaining the apparent prevalence of cold gas even in the extreme outskirts of galaxy haloes.

ACKNOWLEDGEMENTS

We thank Andrey Kravtsov and Eliot Quataert for insightful conversations and suggestions and for detailed comments on the manuscript. We are grateful to Crystal Martin and Mark Dijkstra for interesting conversations, which shaped the early development of this work. We are also grateful to Anna Barnacka, Cara Battersby, Joe Hennawi, Chris McKee, Eve Ostriker, Jim Stone, Drummond Fielding and James Guillochon for interesting and helpful conversations. Drummond Fielding generously helped run a parameter study of the simulations shown in Fig. 4. MM and SPO were supported by NASA grants NNX15AK81G and HST-AR-14307.001-A. MM was also partially supported by NASA grant HST-HF2-51376.001-A, under NASA contract NAS5-26555. SPO thanks KITP for hospitality; this research was supported in part by the National Science Foundation under Grant No. NSF PHY11-25915. RMO acknowledges the support provided by NSF grant AST-1313021. A-MM was partially supported by a TAC fellowship at UC Berkeley's Theoretical Astrophysics Center. We ran our simulations on the Stampede supercomputer, under XSEDE grants TG-AST140047 and TG-AST140083. XSEDE is supported by National Science Foundation grant number ACI-1053575. The authors acknowledge the Texas Advanced Computing Center (TACC) at The University of Texas at Austin for providing resources that have contributed to the research results reported within this paper. We made all of our plots using the open-source software Tioga, and this research made use of NASA's ADS system.

REFERENCES

- Anderson M. E., Churazov E., Bregman J. N., 2015, *MNRAS*, 452, 3905
 Arav N., Barlow T. M., Laor A., Blandford R. D., 1997, *MNRAS*, 288, 1015
 Arnaud M., Pratt G. W., Bohringer H., Croston J. H., Pointecouteau E., 2010, *A&A*, 517, A92
 Arrigoni Battaia F. et al., 2012, *A&A*, 543, A112
 Arrigoni Battaia F., Hennawi J. F., Prochaska J. X., Cantalupo S., 2015, *ApJ*, 809, 163
 Audit E., Hennebelle P., 2005, *A&A*, 433, 1
 Balbus S. A., McKee C. F., 1982, *ApJ*, 252, 529
 Bale S. D., Kasper J. C., Quataert E., Salem C., Sundkvist D., 2009, *Phys. Rev. Lett.*, 103, 211101
 Bale S. D., Pulupa M., Salem C., Chen C. H. K., Quataert E., 2013, *ApJ*, 769, L22
 Banda-Barragán W. E., Parkin E. R., Federrath C., Crocker R. M., Bicknell G. V., 2016, *MNRAS*, 455, 1309
 Bauermeister A., Blitz L., Ma C.-P., 2010, *ApJ*, 717, 323
 Becker G. D., Bolton J. S., 2013, *MNRAS*, 436, 1023
 Ben Bekhti N., Richter P., Westmeier T., Murphy M. T., 2008, *A&A*, 487, 583
 Ben Bekhti N., Richter P., Winkel B., Kenn F., Westmeier T., 2009, *A&A*, 503, 483
 Ben Bekhti N., Winkel B., Richter P., Kerp J., Klein U., Murphy M. T., 2012, *A&A*, 542, A110
 Birnboim Y., Dekel A., 2003, *MNRAS*, 345, 349
 Blagrove K., Martin P. G., Joncas G., Kothes R., Stil J. M., Miville-Deschênes M. A., Lockman Felix J., Taylor A. R., 2017, *ApJ*, 834, 126
 Bonnell I. A., Bate M. R., Vine S. G., 2003, *MNRAS*, 343, 413
 Borisova E. et al., 2016, *ApJ*, 831, 39
 Bottorff M., Ferland G., Baldwin J., Korista K., 2000, *ApJ*, 542, 644
 Braun R., Kanekar N., 2005, *A&A*, 436, L53
 Brüggén M., Scannapieco E., 2016, *ApJ*, 822, 31
 Burkert A., Lin D. N. C., 2000, *ApJ*, 537, 270
 Cai Z. et al., 2017, *ApJ*, 837, 71
 Cantalupo S., 2010, *MNRAS*, 403, L16
 Cantalupo S., Arrigoni-Battaia F., Prochaska J. X., Hennawi J. F., Madau P., 2014, *Nature*, 506, 63
 Churchill C. W., Mellon R. R., Charlton J. C., Vogt S. S., 2003, *ApJ*, 593, 203
 Cooper J. L., Bicknell G. V., Sutherland R. S., Bland-Hawthorn J., 2009, *ApJ*, 703, 330
 Cowie L. L., McKee C. F., 1977, *ApJ*, 211, 135
 Crighton N. H. M., Hennawi J. F., Prochaska J. X., 2013, *ApJ*, 776, L18
 Crighton N. H. M., Hennawi J. F., Simcoe R. A., Cooksey K. L., Murphy M. T., Fumagalli M., Prochaska J. X., Shanks T., 2015, *MNRAS*, 446, 18
 Crutcher R. M., Wandelt B., Heiles C., Falgarone E., Troland T. H., 2010, *ApJ*, 725, 466
 D'Odorico V., Cristiani S., Romano D., Granato G. L., Danese L., 2004, *MNRAS*, 351, 976
 Dietrich M., Wagner S. J., Courvoisier T. J.-L., Bock H., North P., 1999, *A&A*, 351, 31
 Dijkstra M., Gronke M., Venkatesan A., 2016, *ApJ*, 828, 71
 Elvis M., 2000, *ApJ*, 545, 63
 Fang T., Bullock J., Boylan-Kolchin M., 2013, *ApJ*, 762, 20
 Faucher-Giguère C.-A., Quataert E., Murray N., 2012, *MNRAS*, 420, 1347
 Faucher-Giguère C.-A., Feldmann R., Quataert E., Kereš D., Hopkins P. F., Murray N., 2016, *MNRAS*, 461, L32
 Field G. B., 1965, *ApJ*, 142, 531
 Field G. B., Goldsmith D. W., Habing H. J., 1969, *ApJ*, 155, L149
 Fielding D., Quataert E., McCourt M., Thompson T. A., 2017, *MNRAS*, 466, 3810
 Finn C. W. et al., 2014, *MNRAS*, 440, 3317
 Fumagalli M., Hennawi J. F., Prochaska J. X., Kasen D., Dekel A., Ceverino D., Primack J., 2014, *ApJ*, 780, 74
 Gardiner T. A., Stone J. M., 2008, *J. Comput. Phys.*, 227, 4123
 Genzel R. et al., 2010, *MNRAS*, 407, 2091
 Gnedin N. Y., Hollon N., 2012, *ApJS*, 202, 13
 Gritton J. A., Shelton R. L., Kwak K., 2014, *ApJ*, 795, 99
 Hacar A., Tafalla M., 2011, *A&A*, 533, A34
 Hacar A., Tafalla M., Kauffmann J., Kovács A., 2013, *A&A*, 554, A55
 Hacker T. L., Brunner R. J., Lundgren B. F., York D. G., 2013, *MNRAS*, 434, 163
 Hamann F., Barlow T. A., Beaver E. A., Burbidge E. M., Cohen R. D., Junkkarinen V., Lyons R., 1995, *ApJ*, 443, 606
 Hamann F., Kanekar N., Prochaska J. X., Murphy M. T., Ellison S., Malec A. L., Milutinovic N., Ubachs W., 2013, *MNRAS*, 410, 1957
 Hamann F., Chartas G., McGraw S., Rodriguez H. P., Shields J., Capellupo D., Charlton J., Eracleous M., 2013, *MNRAS*, 435, 133

- Hansen M., Oh S. P., 2006, *MNRAS*, 367, 979
- Hennawi J. F., Prochaska J. X., Cantalupo S., Arrighi-Battaia F., 2015, *Science*, 348, 779
- Hennebelle P., Audit E., 2007, *A&A*, 465, 431
- Hennebelle P., Péroul M., 1999, *A&A*, 351, 309
- Hitomi Collaboration, Aharonian F. et al., 2016, *Nature*, 535, 117
- Jeans J. H., 1901, *Proc. R. Soc. Lond. Ser. I*, 68, 454
- Ji S., Oh S. P., McCourt M., 2017, *MNRAS*, preprint ([arXiv:1710.00822](https://arxiv.org/abs/1710.00822))
- Kannan R. et al., 2014, *MNRAS*, 437, 2882
- Kereš D., Katz N., Weinberg D. H., Davé R., 2005, *MNRAS*, 363, 2
- Klein R. I., McKee C. F., Colella P., 1994, *ApJ*, 420, 213
- Komarov S. V., Churazov E. M., Kunz M. W., Schekochihin A. A., 2016, *MNRAS*, 460, 467
- Koyama H., Inutsuka S.-i., 2002, *ApJ*, 564, L97
- Kuhlen M., Faucher-Giguère C.-A., 2012, *MNRAS*, 423, 862
- Kunz M. W., Schekochihin A. A., Stone J. M., 2014, *Phys. Rev. Lett.*, 112, 205003
- Kwak K., Henley D. B., Shelton R. L., 2011, *ApJ*, 739, 30
- Lau M. W., Prochaska J. X., Hennawi J. F., 2016, *ApJS*, 226, 25
- Lazarian A., 2014, *Space Sci. Rev.*, 181, 1
- Lecoanet D. et al., 2016, *MNRAS*, 455, 4274
- Liang C. J., Kravtsov A. V., Agertz O., 2016, *MNRAS*, 458, 1164
- Low C., Lynden-Bell D., 1976, *MNRAS*, 176, 367
- Mac Low M.-M., McKee C. F., Klein R. I., Stone J. M., Norman M. L., 1994, *ApJ*, 433, 757
- Maller A. H., Bullock J. S., 2004, *MNRAS*, 355, 694
- Mandelker N., Padnos D., Dekel A., Birnboim Y., Burkert A., Krumholz M. R., Steinberg E., 2016, *MNRAS*, 463, 3921
- Markevitch M., Vikhlinin A., 2007, *Phys. Rep.*, 443, 1
- Martin C. L., 2005, *ApJ*, 621, 227
- Martin C. L., Dijkstra M., Henry A., Soto K. T., Danforth C. W., Wong J., 2015, *ApJ*, 803, 6
- McCourt M., Sharma P., Quataert E., Parrish I. J., 2012, *MNRAS*, 419, 3319
- McCourt M., O’Leary R. M., Madigan A.-M., Quataert E., 2015, *MNRAS*, 449, 2
- Meerson B., 1989, *ApJ*, 347, 1012
- Mellema G., Kurk J. D., Röttgering H. J. A., 2002, *A&A*, 395, L13
- Miville-Deschênes M.-A. et al., 2017, *A&A*, 599, A109
- Nagai D., Vikhlinin A., Kravtsov A. V., 2007, *ApJ*, 655, 98
- Nelson D., Vogelsberger M., Genel S., Sijacki D., Kereš D., Springel V., Hernquist L., 2013, *MNRAS*, 429, 3353
- Netzer H., 2006, in Alloin D., ed., *Lecture Notes in Physics*, Vol. 693, *Physics of Active Galactic Nuclei at All Scales*. Springer Verlag, Berlin, p. 1
- Neufeld D. A., 1991, *ApJ*, 370, L85
- Oppenheimer B. D., Dav R., Kere D., Fardal M., Katz N., Kollmeier J. A., Weinberg David H., 2010, *MNRAS*, 406, 2325
- Planck Collaboration XI, 2013, *A&A*, 557, A52
- Prescott M. K. M., Martin C. L., Dey A., 2015, *ApJ*, 799, 62
- Prochaska J. X., Hennawi J. F., 2009, *ApJ*, 690, 1558
- Prochaska J. X., Hennawi J. F., Simcoe R. A., 2013, *ApJ*, 762, L19
- Rauch M., Sargent W. L. W., Barlow T. A., 1999, *ApJ*, 515, 500
- Read J. I., Hayfield T., Agertz O., 2010, *MNRAS*, 405, 1513
- Rees M. J., 1987, *MNRAS*, 228, 47P
- Richter P., 2006, in Roeser S., ed., *Reviews in Modern Astronomy*, Vol. 19, *Reviews in Modern Astronomy*. Wiley-VCH Verlag, Weinheim, Germany, p. 31
- Richter P., 2012, *ApJ*, 750, 165
- Richter P. et al., 2001, *ApJ*, 559, 318
- Richter P., Sembach K. R., Howk J. C., 2003, *A&A*, 405, 1013
- Richter P., Westmeier T., Brüns C., 2005, *A&A*, 442, L49
- Richter P., Charlton J. C., Fangano A. P. M., Bekhti N. B., Masiero J. R., 2009, *ApJ*, 695, 1631
- Rigby J. R., Charlton J. C., Churchill C. W., 2002, *ApJ*, 565, 743
- Rudie G. C. et al., 2012, *ApJ*, 750, 67
- Scannapieco E., Brüggemann M., 2015, *ApJ*, 805, 158
- Schaye J., Carswell R. F., Kim T.-S., 2007, *MNRAS*, 379, 1169
- Schneider E. E., Robertson B. E., 2017, *ApJ*, 834, 144
- Schunk R. W., Hays P. B., 1971, *Planet. Space Sci.*, 19, 113
- Schwartz C. M., Martin C. L., 2004, *ApJ*, 610, 201
- Shang C., Oh S. P., 2012, *MNRAS*, 426, 3435
- Shapiro P. R., Field G. B., 1976, *ApJ*, 205, 762
- Sharma P., Hammett G. W., Quataert E., Stone J. M., 2006, *ApJ*, 637, 952
- Sharma P., McCourt M., Parrish I. J., Quataert E., 2012, *MNRAS*, 427, 1219
- Shin M.-S., Stone J. M., Snyder G. F., 2008, *ApJ*, 680, 336
- Shull J. M., Jones J. R., Danforth C. W., Collins J. A., 2009, *ApJ*, 699, 754
- Siana B. et al., 2010, *ApJ*, 723, 241
- Sparks W. B., Pringle J. E., Donahue M., Carswell R., Voit M., Cracraft M., Martin R. G., 2009, *ApJ*, 704, L20
- Stern J., Hennawi J. F., Prochaska J. X., Werk J. K., 2016, *ApJ*, 830, 87
- Stoeckle J. T., Keeney B. A., Danforth C. W., Shull J. M., Froning C. S., Green J. C., Penton S. V., Savage B. D., 2013, *ApJ*, 763, 148
- Stone J. M., Gardiner T. A., Teuben P., Hawley J. F., Simon J. B., 2008, *ApJS*, 178, 137
- Sutherland R. S., Dopita M. A., 1993, *ApJS*, 88, 253
- Suzuki-Vidal F. et al., 2015, *ApJ*, 815, 96
- Thompson T. A., Quataert E., Zhang D., Weinberg D. H., 2016, *MNRAS*, 455, 1830
- Townsend R. H. D., 2009, *ApJS*, 181, 391
- van de Voort F., Schaye J., Booth C. M., Haas M. R., Dalla Vecchia C., 2011, *MNRAS*, 414, 2458
- Voit G. M., Donahue M., 1990, *ApJ*, 360, L15
- Voit G. M., Bryan G. L., O’Shea B. W., Donahue M., 2015, *ApJ*, 808, L30
- Wakker B. P., van Woerden H., 1997, *ARA&A*, 35, 217
- Werk J. K. et al., 2014, *ApJ*, 792, 8
- White S. D. M., Rees M. J., 1978, *MNRAS*, 183, 341
- Wiersma R. P. C., Schaye J., Smith B. D., 2009, *MNRAS*, 393, 99
- Wiener J., Oh S. P., Zweibel E., 2017, *MNRAS*, 467, 646
- Yoon J. H., Putman M. E., Thom C., Chen H.-W., Bryan G. L., 2012, *ApJ*, 754, 84
- Zhang D., Thompson T. A., Quataert E., Murray N., 2017, *MNRAS*, 468, 4801
- Zheng Y., Putman M. E., Peek J. E. G., Joung M. R., 2015, *ApJ*, 807, 103
- ZuHone J. A., Markevitch M., Ruszkowski M., Lee D., 2013, *ApJ*, 762, 69

APPENDIX A: SIMULATION SET-UP

This section details our computational method. In all of our simulations, we integrate the usual equations of ideal hydrodynamics using the conservative code Athena (Gardiner & Stone 2008; Stone et al. 2008). In order to ensure that we resolve the dynamics in the wakes of disrupting clouds, we use a fixed Cartesian grid with equal resolution throughout the domain. Simulations of multiphase gas contain very high Mach numbers and sharp density gradients; since this combination makes conservative codes prone to crashes, we use the ‘van Leer’ integrator implemented in Athena, with second-order reconstruction in primitive variables. This choice is more diffusive, and hence more robust, than the Athena’s default integrator. We have checked that shattering still happens with the CTU integrator with third-order reconstruction; if anything, we suspect our choice overestimates mixing and the destruction of cold cloudlets.

We note that every simulation in this paper assumes ideal hydrodynamics and is two-dimensional; we discuss these significant limitations in Appendix B and in Section 4.1.

By construction, in many of our simulations the cooling time of the gas becomes very short compared to the dynamical time. This is expensive to simulate using methods which add cooling as a source term to the integrator, as these methods limit the simulation time-step to a small fraction of the cooling time. Instead, we implemented the ‘exact’ cooling algorithm described in Townsend (2009), which rewrites the operator-split energy equation as

$$t_{\text{cool}} \frac{dT}{dt} = -T_0 \frac{\Lambda(T)}{\Lambda(T_0)}, \quad (\text{A1})$$

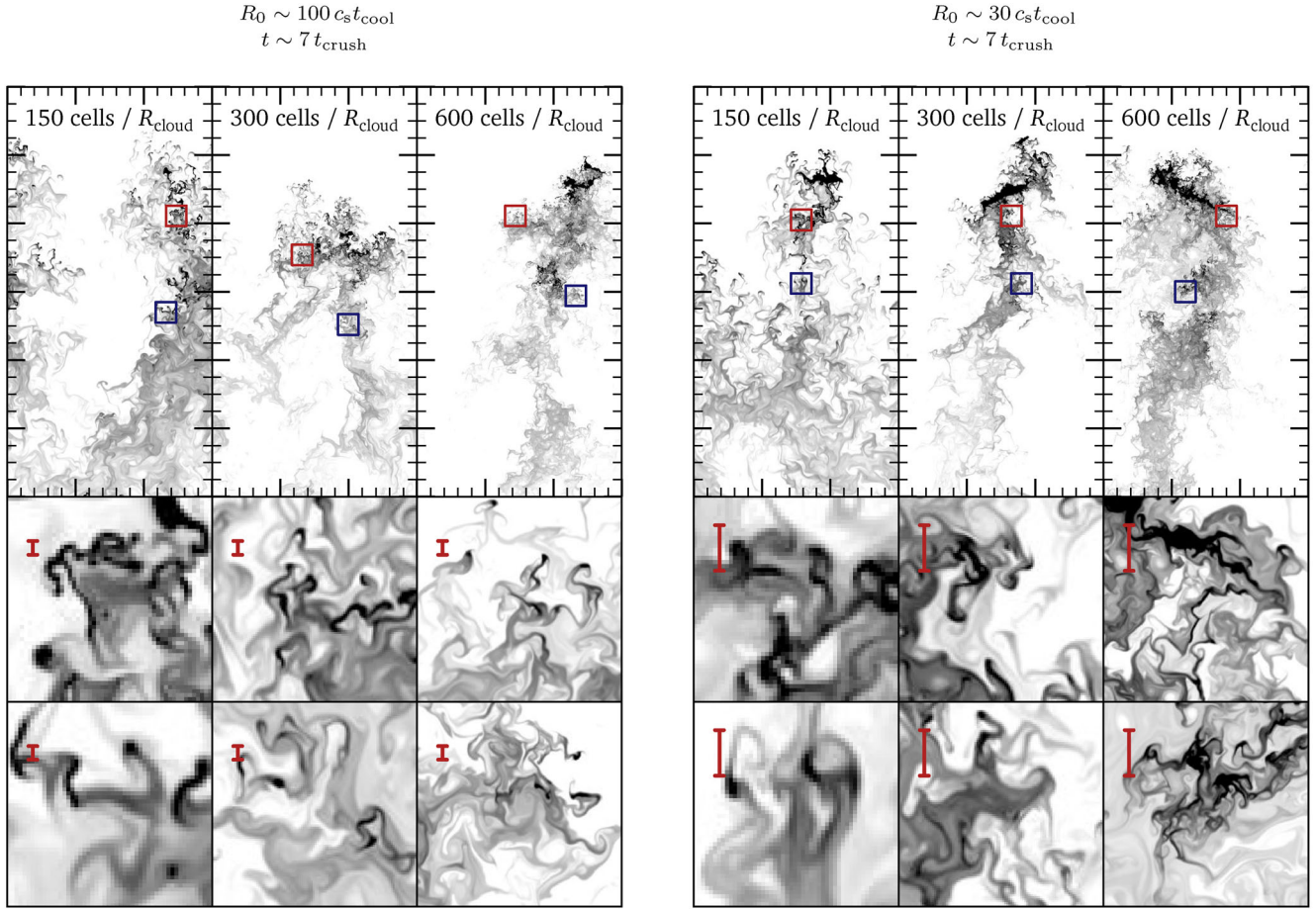


Figure A1. Resolution studies for ‘cloud crushing’ simulations shown in Fig. 5. The *left-hand* plot shows a simulation with an initial cloud size $R_0 \sim 100 c_s t_{\text{cool}}$ (second from the right in Fig. 5), and the *right-hand* plot shows a simulation with an initial cloud size $R_0 \sim 30 c_s t_{\text{cool}}$ (not shown in Fig. 5). We show simulations with resolutions of 150, 300 and 600 cells per cloud radius; we show simulations with a resolution of 300 cells/ R_{cloud} in the rest of our figures. As in Fig. 5, the squares (red, top; blue, bottom) mark regions shown in the insets below; zooming in reveals that the apparently wispy regions in the wakes behind the clouds are in fact filled with small dense knots of cold gas. The simulations do not converge, are not expected to since they contain unresolved gradients and do not include explicit dissipation; however, the knots of cold gas appear to track the lengthscale $c_s t_{\text{cool}}$, marked in the insets with a red error bar.

where T_0 is the temperature at the start of a time-step. Townsend (2009) solves equation A1 by separating variables. This integral has a closed-form solution for piecewise power-law cooling curves $\Lambda(T)$ such as our fit to the Sutherland & Dopita (1993) curve shown in Fig. 2, enabling an efficient and accurate representation of cooling, even for very short cooling times.

Since it is already computationally expensive to resolve the scale $c_s t_{\text{cool}}$, we apply a temperature floor at 10^4 K to prevent cloudlets from cooling further and contracting to yet smaller scales. Cooling below 10^4 K must be addressed in a future study.

A1 Thermal instability simulations

The simulations are shown in Fig. 4. We begin with a domain in which $\rho \sim 1$ and $T \sim 1$. We chose our unit system such that this corresponds to diffuse gas with a density $n \sim 10^{-4} \text{ cm}^{-3}$ and $T \sim 10^7$ K. We use a high temperature such that this gas has a long cooling time and we do not need to include heating or feedback processes to maintain an ambient hot phase.

We generate a Gaussian-random scalar field δ which has a power spectrum $\propto k^{-1}$ over a range of scales from $k \sim 2\pi/L$ to $k \sim 40 \times 2\pi/L$, where L is the smallest size of the domain. We

normalize the scalar field δ to have an RMS of unity and then apply the density perturbation:

$$\rho \rightarrow \rho \times e^{2+\delta}, \quad (2a)$$

followed by the correction

$$\rho = \begin{cases} \rho, & \rho \leq 10 \\ 10 + \sqrt{\rho - 10}, & \rho > 10, \end{cases} \quad (2b)$$

which effectively flattens the high-density regions, preventing mass from concentrating in a small fraction of the domain. We perturb density but not pressure, so that the temperature $T \propto 1/\rho$. This arbitrary perturbation generates the initial condition shown in Fig. 4: roughly half of the domain is at $\sim 10^6$ K, with a density of $\rho \sim 10$. While this set-up may seem contrived, it ensures that (i) we do not seed the simulation with tiny-scale structure such as shattering might produce, and (ii) that the perturbation occupies a large volume, making it easier to resolve. We do not expect our results to be very sensitive to this initial perturbation, but will investigate in more detail in a future study.

We run our simulations for ~ 1 cooling time in the 10^6 K gas, and scale the domain to $L \sim 10^5 \times c_s t_{\text{cool}}$ (top), $L \sim 10^3 \times c_s t_{\text{cool}}$ (middle) and $L \sim 10 \times c_s t_{\text{cool}}$ (bottom). Since we run for a fixed

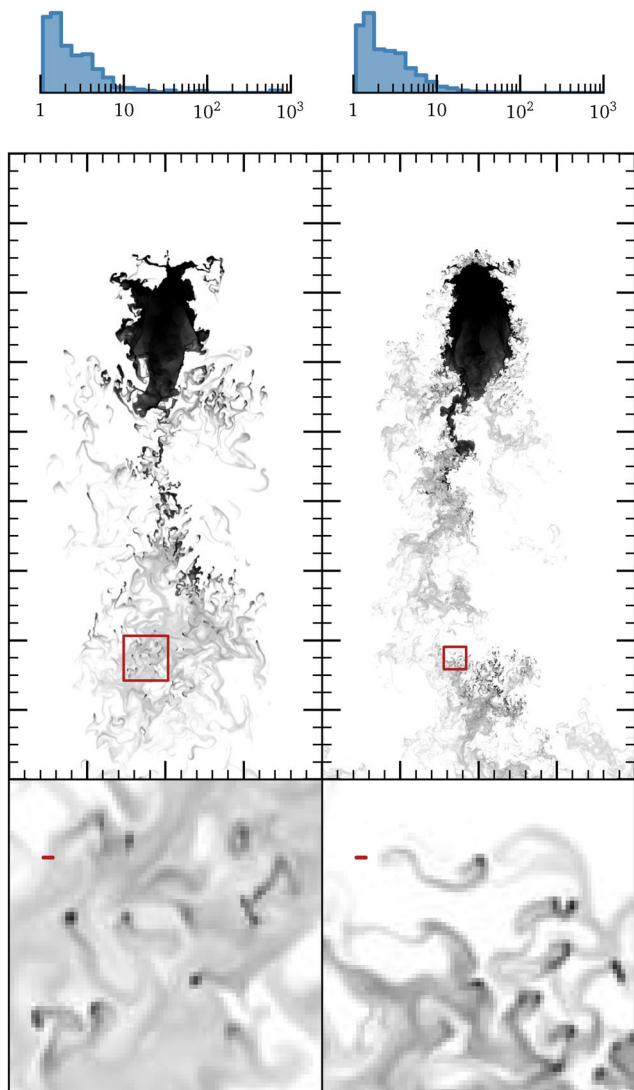


Figure A2. Clump formation in unresolved simulations with an initial cloud size $R_0 = 10^4 c_s t_{\text{cool}}$. Mixed, $\sim 10^5$ K gas in the wake of the cloud is thermally unstable and rapidly cools to form small clumps of cold gas. These clumps form at roughly the grid scale of the simulation: higher resolution simulations produce more, and increasingly smaller, clumps. The clump size histograms shown at the top are essentially identical when put in units of the cell size; increasing the resolution by a factor of 4 (from 150 cells per cloud radius to 600) simply decreased all of the clump size by the same factor. In both simulations, the clump sizes are therefore consistent with zero; they are totally unresolved.

cooling time, simulations with small domain sizes are much more expensive due to the short sound-crossing time. We therefore use a resolution of (4096×2048) , (512×256) and (256×128) for the simulations. The different behaviour is not simply due to the differing resolutions, however; we do see shattering even in lower-resolution simulations of big clouds.

A2 Cloud crushing simulations

These simulations are shown in Figs 5, A1, A2 and A3.

This set-up is essentially identical to the one used in McCourt et al. (2015), except that we do not use magnetic fields and we run our simulations in 2D. Following Shin, Stone & Snyder (2008), we

use a passively advected scalar to keep track of the cloud and we boost the simulation domain after every time-step to keep the cloud from leaving the boundaries. This technique both decreases the size of the computational grid needed to track the cloud material and reduces the truncation errors by minimizing the relative velocity between the cloud and the computational grid.

In all of our simulations except those in the bottom panel of Fig. A3, we impose a steady wind with $v_x = 1.5 c_s$ at the upstream boundary, where c_s is the sound speed in the external, confining medium. This velocity seems appropriate for dense clouds free-falling through hot virialized gas, as might be found in the CGM or in galactic winds. Fig. A3 shows that our results are not sensitive to the particular choice, however. We use an outflow (zero-gradient) boundary condition downstream, and periodic boundary conditions in the directions orthogonal to the flow. We choose periodic boundary conditions for their simplicity and numerical stability.

These simulations have domain sizes of $(6.666 \times 26.666) R_{\text{cloud}}$; i.e., with an aspect ratio of 4:1. We show only the upper half of the domain in these figures. Unless otherwise specified, these simulations have a resolution of $(300 \text{ cells})/R_{\text{cloud}}$, or (2048×8192) cells across the domain.

A3 Entrainment simulations

The simulation shown in Fig. 6 uses a set-up essentially identical to that in Fig. 5, however the background is at 10^6 K instead of 10^7 K and the cold gas is distributed in a large number of small chunks rather than in a single, monolithic entity. We use a resolution of (4096×16384) cells across the domain, such that each cloudlet is resolved with $(64)^2$ cells. Each cloudlet has a size $\sim 10 \times c_s t_{\text{cool}}$. Since this simulation runs for a time-scale longer than the cooling time in the ambient hot gas, we add a crude form of ‘feedback’ heating in order to maintain a well-defined hot phase: after every call of Townsend (2009)’s integrator, we take the total thermal energy lost to cooling and add it back into the domain at a constant rate per unit volume.

APPENDIX B: NUMERICAL UNCERTAINTIES AND COMPARISON TO PREVIOUS WORK

The dynamics of multiphase gas is unfortunately difficult to simulate reliably: both SPH-type codes and Godunov-type codes have severe problems modelling the contact discontinuities separating the hot and cold phases (e.g. Read, Hayfield & Agertz 2010; Lecoanet et al. 2016). Numeric errors can either enhance or suppress mixing between hot and cold gas, and very little experimental data is available to confirm numerical results in the regimes relevant to astrophysical multiphase gas (with $\delta\rho/\rho \gg \{\delta P/P, 1\}$ and $\text{Re} \gg 1$).

Lecoanet et al. (2016) show that Godunov-type grid codes are susceptible to an artificial instability which likely overestimates cloud destruction and mixing in our simulations; we have made no attempt to control such errors in this paper, however, as it would be prohibitively expensive to do so (even in 2D; shattering is likely not possible in 1D). The possibility of uncontrolled artificial instabilities represents a significant limitation of our simulations which we are currently unable to address. None the less, our basic result that large clouds with short cooling times are prone to fragmentation appears to be robust, even if the details of the cloud disruption in Fig. 5 are not. While the shear instabilities destroying the clouds in Fig. 5 (and especially the numerical errors associated with these instabilities; Lecoanet et al. 2016) depend *strongly* on the density

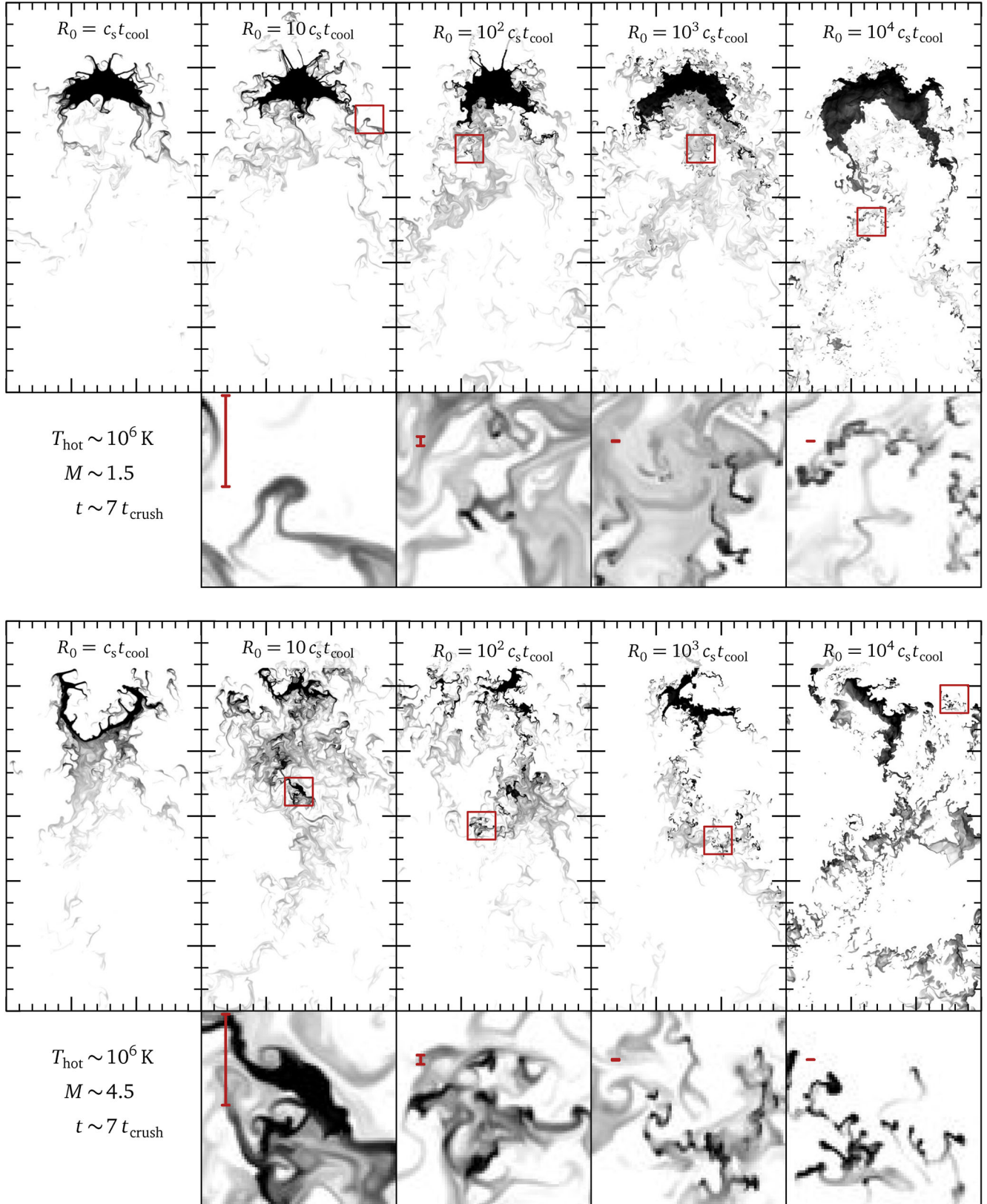


Figure A3. Same as Fig. 5 but for a 10^6 K halo. Though the disruption of the initial cloud proceeds very differently here due to the lower density ratio, the clump size distributions are virtually identical to those in Fig. 5. This strongly suggests that it is the cooling rate and properties of the cold gas which determines the cloud size, rather than the properties of the hot gas as suggested by Burkert & Lin (2000) and Audit & Hennebelle (2005). The lower plot shows a repeat simulation with Mach number ~ 4.5 (i.e., with the same velocity as in Fig. 5). In this case, increasing the Mach number by a factor ~ 3 increases the cloudlet size by a factor ~ 2 , suggesting that heating does play a small role in determining the cloudlet size

ratio between hot and cold gas, we find a lengthscale for cold gas which is independent of this density ratio (cf. Figs 5 and A3). Numeric errors also increase substantially with increasing resolution for the setup shown in Fig. 5 (Lecoanet et al. 2016); however, we find similar cloudlet sizes even at different resolutions (see, e.g., Fig. A1). Moreover, while numeric errors should generically grow at the grid scale, where the time-scale is the fastest, we find shattering takes place at a physical lengthscale, $\sim c_s t_{\text{cool}}$, and time-scale, $\sim t_{\text{cool}}$, which can be resolved if the domain size is made sufficiently small (Figs 4, 5 and A1); this behaviour is expected for a physical process, but not for any known artificial instability due to errors in the method. We furthermore note that we use the van Leer integrator with second-order reconstruction in the simulations shown in this paper (see Appendix A); this is more diffusive than the default integrator implemented in Athena and therefore less susceptible to numeric instabilities. We obtain similar results using Athena's default CTU integrator with third-order reconstruction.

The above remarks suggest that the shattering we highlight in Figs 4, 5 and A3 is not simply the result of an artificial numeric instability, even though such instabilities may be present in our simulations. We also find results suggestive of shattering in a number of previously published simulations; these simulations use a variety of codes and set-ups, and would presumably exhibit different numerical problems. The 2D hydrodynamic simulations in Mellema et al. (2002) and Koyama & Inutsuka (2002), and 3D hydrosimulations in Cooper et al. (2009) and Schneider & Robertson (2017), who all study some variant of the cloud crushing problem, show qualitatively similar fragmentation driven by cooling. This behaviour is also consistent with Audit & Hennebelle (2005) and Hennebelle & Audit (2007), who also find in high-resolution 2D simulations that clouds fragment at the grid scale. (These authors furthermore show that a stable two-phase medium in approximate pressure equilibrium, as we appeal to in Section 2.1, makes sense even in a strongly turbulent flow.) Though Kwak, Henley & Shelton (2011) and Gritton, Shelton & Kwak (2014) do not study fragmentation directly in their simulations of HVCs, it appears from their plots that larger initial cloud sizes are more prone to breaking apart, which is again consistent with our findings here.

Since most previous studies have focused on macroscopically large clouds, with $R_0 \gg c_s t_{\text{cool}}$, we expect the cloudlets are essentially always unresolved in currently published studies. More work is therefore needed to confirm the cloudlet size of $\sim c_s t_{\text{cool}}$ as we find here, and to identify its dependence on parameter choices and on other processes. The impact of magnetic fields on the formation and on the morphologies of these cloudlets will be especially important to study.

The references above suggest that there is precedent for shattering in the astrophysical literature. But if shattering is a general hydrodynamic process, why don't all simulations with cooling show fragmentation to the grid scale? We suspect this is because shattering is particularly sensitive to numerical resolution. In Fig. A2, the blue histograms above each column show clump size distributions¹⁹ in terms of the cell size of the simulation grid. The distribution in the leftmost panel represents unresolved clumps in which fragmentation

is determined by grid-scale effects; we confirmed this by re-running this simulation with $4 \times$ higher resolution, obtaining the exact same distribution in units of the cell size. *We note that, surprisingly, even clumps with sizes of ~ 10 cells (100 cells in area) are entirely unresolved*; though these clumps seem much larger than the grid scale, we find the size is proportional to the grid cell size when we compare simulations with different resolutions. The fragmentation of clumps up to ~ 10 cells in size is therefore entirely determined by grid-scale effects. Thus, we expect that only fragments with a size $\gtrsim 20$ cells are capable of splitting – though this exact cut-off depends on the numeric method used, we expect it is typical of the astrophysical grid codes in current use. In our simulations, we find a resolution of $\gtrsim 150$ cells per cloud radius is necessary to see the repeated fragmentation leading to shattering in 2D. (However this requirement seems to be somewhat lower in 3D; O'Leary et al., in preparation) Since cloud-crushing simulations typically have resolutions of 32–64 cells per cloud radius (e.g. McCourt et al. 2015; Scannapieco & Brügger 2015), this may not be sufficient to see the shattering we discuss here. In recent years, however, a few 3D simulations have been published approaching the required resolution (Scannapieco & Brügger 2015; Banda-Barragán et al. 2016; Brügger & Scannapieco 2016; Schneider & Robertson 2017, e.g.).

Audit & Hennebelle (2005) and Burkert & Lin (2000) present very high resolution simulations with cooling, which should in principle exhibit shattering. The high-resolution 2D simulations in Audit & Hennebelle (2005) do show rapid fragmentation to the grid scale, representing an upper limit since they were not designed to resolve the scales discussed here. The 1D simulations in Burkert & Lin (2000) study only purely single-mode perturbations. These single-mode simulations enable an impressive and thorough analysis in Burkert & Lin (2000), but may impose too much symmetry to fragment in the manner discussed here; it is also unclear whether fragmentation is possible in 1D. Moreover, the simulations in Burkert & Lin (2000) run only for ~ 1 cooling time, and so do not follow the full non-linear evolution. It is likely that shattering happens on a somewhat longer time-scale (though still short compared to the dynamical time).

Finally, we note that the scale $\sim c_s t_{\text{cool}}$ is only accurate to within an order of magnitude. It scales (crudely) as $\sim T^3$ above 10^4 K, so heating the clouds only slightly above the temperature at which $c_s t_{\text{cool}}$ is minimized could make them substantially larger. When we increase the Mach number of the cloud by a factor of 3, we find cloudlets which are larger by a factor of $\lesssim 2$, suggesting that heating does in fact play a secondary role in determining the final cloud size (see Fig. A3). Though this is an interesting possibility, we unfortunately cannot confidently pursue it here. As discussed in Section 4.1, these simulations omit a number of potentially important physical processes. We will consider these in future work.

¹⁹ We define 'clumps' as contiguous blocks of cells with a density \geq half the density of the initial cloud. In these 2D simulations, we quote the clump size as the square root of the area, measured in units of grid cells.